Nanoscale

ROYAL SOCIETY OF CHEMISTRY

MINIREVIEW

View Article Online
View Journal | View Issue

Cite this: *Nanoscale*, 2021, **13**, 19840

Recent advances in the heteroatom doping of perovskite oxides for efficient electrocatalytic reactions

Yifan Liu,† Honglan Huang,† Liang Xue, Jingwen Sun, Xin Wang, Pan Xiong * and Junwu Zhu*

Perovskite-type transition metal oxides have emerged as promising electrocatalysts for various electrocatalytic reactions owing to their low cost, compositional tunability and high stability. However, insufficient electrocatalytic activities of pristine perovskite oxides hinder their pathway towards real-world applications. The incorporation of heteroatoms into perovskite oxide structures has been regarded as an efficient way to improve the electrocatalytic performance. This minireview summarizes the recent advances in the heteroatom doping of perovskite oxides as efficient electrocatalysts for the hydrogen evolution reaction (HER), oxygen evolution reaction (OER) and oxygen reduction reaction (ORR). These heteroatom doping strategies are classified based on various types of doping sites. The mechanisms of improved electrocatalytic activities are discussed in detail within different doping sites and various kinds of dopants. Finally, the remaining challenges and perspectives are outlined for future developments of perovskite oxide-based catalysts.

Received 3rd September 2021,
Accepted 9th November 2021

DOI: 10.1039/d1nr05797a

rsc.li/nanoscale

1. Introduction

With the accelerated depletion of fossil fuels and environmental issues, advanced energy conversion technologies have attracted considerable attention in academia and industry.[1–9] Among them, energy conversion based on electrocatalytic reactions is a promising strategy, which can convert energies efficiently and flexibly through chemical bond transitions.[10–13] Although noble metal (*e.g.*, Pt, Ir, Ru, Pd, and Rh) based cata-

Key Laboratory for Soft Chemistry and Functional Materials of Ministry Education, School of Chemistry and Chemical Engineering, Nanjing University of Science and Technology, Nanjing, 210094, China. E-mail: pan.xiong@njust.edu.cn, zhujw@njust.edu.cn

†These authors contributed equally.

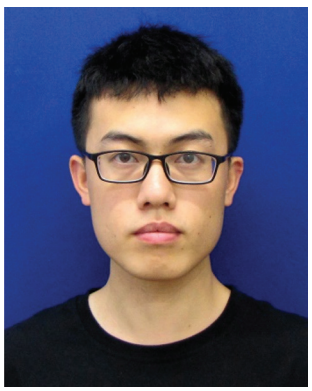

Yifan Liu

Yifan Liu received his BSc degree in Chemical Engineering from Nanjing Tech University, China, in 2019. He is now pursuing his Ph.D. degree under the supervision of Professor Junwu Zhu in the School of Chemistry and Chemical Engineering at Nanjing University of Science and Technology, China. His research focuses on perovskite oxide nanomaterials for electrocatalytic applications.

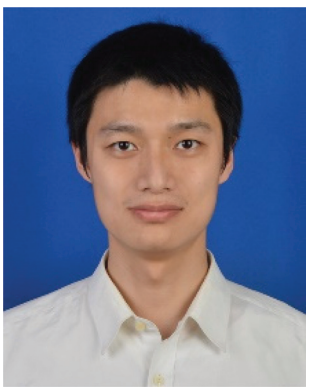

Honglan Huang

Honglan Huang received his BSc degree in Chemistry both from Nanjing Tech University and the University of Sheffield in 2018, and MRes degree in Nanomaterials in Imperial College London under the supervision of Dr James E. M. Lewis. Currently, he is pursuing his Ph. D. degree under the supervision of Professor Junwu Zhu in the School of Chemistry and Chemical Engineering at Nanjing University of Science and Technology. His current research focuses on the design of solid-state electrolytes for lithium metal batteries.

lysts have been widely used for electrochemical and renewable energy technologies,[14–17] their prohibitive cost and extreme scarcity hindered their large-scale applications in the energy conversion industry. Therefore, it is imperative to seek low-cost and Earth-abundant alternative catalysts with comparable electrocatalytic activities for commercial demands.[4,18–24]

Perovskite-type transition metal oxides with a general formula of ABO_3 show high compositional tunability, where the A-site is generally occupied by a rare-earth/alkaline metal with 12-fold coordination and the B-site is occupied by a transition metal with 6-fold coordination with O atoms.[25] Due to their low cost, environmental friendliness, high catalytic stability and large potential window, perovskite oxides have been intensively studied as promising catalysts for multiple electrocatalytic reactions, such as the hydrogen evolution reaction (HER), oxygen evolution reaction (OER), oxygen reduction reaction (ORR), carbon dioxide reduction reaction (CO_2RR), and nitrogen reduction reaction (NRR).[26–30] However, in most instances, the catalytic activities of perovskite oxides are incomparable to those of conventional noble metal catalysts. This is because disunited 3d orbitals of surface transition metal cations usually result in either too weak or too strong surface adsorption/desorption strength of reactants.[31] Meanwhile, the relatively low electrical conductivities of many perovskite oxides lead to a sluggish charge-transfer process and slow the electrocatalytic kinetics.[32] To curb these adverse factors, many strategies have been attempted to improve the electrocatalytic performance of perovskite oxide catalysts, including heteroatom doping,[33,34] interfacial engineering,[35] strain modulation,[36,37] and introduction of defects.[38,39]

Among these strategies, heteroatom doping is one of the most facile and effective methods to optimize the catalytic properties of perovskite oxides. By affecting the interaction between oxygen and B-site atoms, the doped heteroatoms can improve the coupling efficiency of active centers and intermediate reactants, leading to facilitated electrocatalytic reactions.[40] In terms of the elemental composition of perovskite oxides, in principle, more than 30 and 50 kinds of elements in the periodic table have been found at the A- and B-sites in ABO_3 perovskite oxides, respectively.[25] The great flexibility in composition determines the diversity of doped heteroatoms, which could be doped into different sites of the ABO_3 perovskite oxides, namely, the A-site, B-site, O-site, and dual-sites. This results in various optimizing concepts, such as A-site doping can impact indirectly *via* activating the transition metal catalytic sites,[41,42] B-site doping can optimize the B-site catalytic activities *via* electron exchange between the heteroatoms and the intrinsic B-site cations of perovskite oxides,[43,44] O-site doping can create abundant oxygen vacancies to improve the electrical conductivity,[45,46] and dual-site doping can promote the multi-active sites synergistically.[47] Recently, various types of dopants have been studied, including heteroatoms doped into the A site (*e.g.*, Na, K, Sr, Ca, Yb, Ce and La),[41,42,48–52] B site (*e.g.*, Ru, Ir, Fe, Co, Ni, Mn, W, P, S and Si),[34,53–59] O site (*e.g.*, F, S, N and Cl),[46,60–62] and dual sites (*e.g.*, Sr&Fe and Fe&Sn).[47,63,64] Although some work on heteroatom-doped strategies for electrocatalysis has been outlined briefly as a branch of optimizing approaches,[45,65,66] a few reports are systematically and comprehensively concerned with reviewing perovskite oxide electrocatalysts from the aspect of different doping sites. An up-to-date summarization of the latest discoveries and achievements is indispensable.

Herein, this minireview focuses on the recent advances in heteroatom doping strategies for the design of perovskite oxides towards efficient electrocatalytic reactions. These heteroatom doping strategies are classified based on the various types of doping sites, namely, A site, B site, O site and dual sites in perovskite oxides. The mechanisms of improved electrocatalytic activity are discussed in detail within different doping sites for three important electrocatalytic reactions, namely, the HER, OER, and ORR (Fig. 1). The current challenges and future perspectives are also outlined. This minire-

Xin Wang

Xin Wang received his PhD degree in inorganic chemistry at the Department of Chemistry, Nanjing University in 1985. After that, he joined Nanjing University of Science and Technology and was promoted to full professor in 1988. His research interests are focused on the design and synthesis of nanostructured materials for use in energy storage and conversion.

Pan Xiong

Pan Xiong is a Professor at the Nanjing University of Science and Technology, China. He received his PhD degree in Materials Science and Engineering from the same university in 2015. He was a visiting PhD student at the University of Texas at Austin followed by working as a postdoctoral researcher at the National Institute for Materials Science (NIMS), Japan and then a research associate at the University of Technology Sydney, Australia. His research focuses on two-dimensional nanomaterials and their heterostructures/superlattices for energy conversion and storage applications.

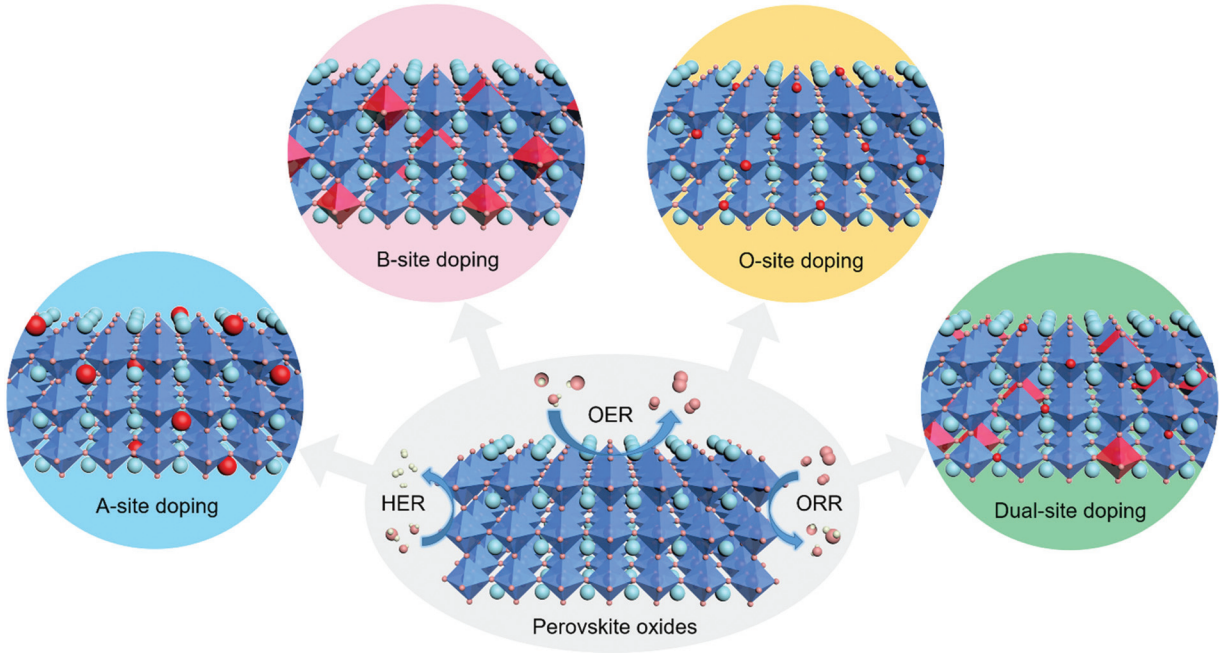

Fig. 1 Schematic illustration of the A-site, B-site, O-site and dual-site heteroatom doping of ABO_3-type perovskite oxides for efficient electrocatalytic reactions including the HER, OER and ORR.

view aims to provide general guidelines and timely viewpoints for the design of highly efficient perovskite oxide catalysts based on heteroatom doping approaches.

2. A-site cation doping

Generally, the A-site cations in the pristine perovskite oxide structures are considered not to participate in the electrocatalytic process.[45] However, it will indirectly affect the electrocatalytic performance *via* activating the transition metal catalytic sites. In previous works, many heteroatoms have been doped into A sites to tailor the electronic structures, and thereby to enhance the electrocatalytic activities of perovskite oxides. Accordingly, the effects of A-site doping in perovskite oxides on the electrocatalytic activities will be summarized based on the categories of doped heteroatoms, including alkali metals (*e.g.*, Na^+ and K^+),[48,49] alkaline-earth metals (*e.g.*, Sr^{2+} and Ca^{2+}),[50,67] and rare-earth metals (*e.g.*, Yb^{3+}, Ce^{3+} and La^{3+}).[41,42,52]

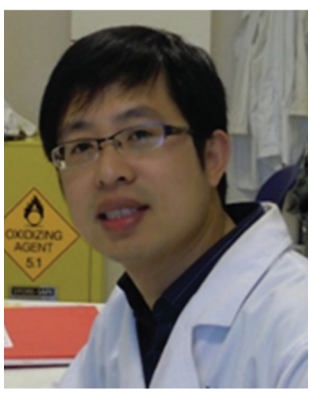

Junwu Zhu

Junwu Zhu received his PhD degree in materials chemistry from the Nanjing University of Science and Technology in 2005. He is presently working as a professor at the same university. His main research interests are focused on the preparation and application of functional materials based on carbon and nanostructured composites.

2.1 A-site doping with alkali metals

Acting as p-type dopants, alkali metals usually have a lower valence of +1 and smaller size than the A-site cations of perovskite oxides. Among them, Na^+ and K^+ are widely adopted to modify the A-site and tailor the properties of perovskite oxides both physically and chemically. For example, the significant volumetric mismatch between Na^+/K^+ dopants and A-site metal cations of perovskite oxides will result in lattice rearrangements.[48] Besides, the alkali metal dopants with a lower valence than the A-site metal cations in perovskite oxides will increase oxygen vacancies or change the oxidation state of B-site active centers owing to charge compensation effects.[67] All of these structural changes can effectively manipulate the electrocatalytic activity and durability.

Pavone *et al.* proposed K-doped $Sr_2Fe_{1.5}Mo_{0.5}O_6$ (KSFMO) (Fig. 2a) as an excellent bifunctional catalyst for both the OER and ORR *via* first principles calculations.[48] They analyzed the structural and electronic features of both $Sr_{1.5}Fe_{1.5}Mo_{1.5}O_6$ (SFMO) and KSFMO. In the SFMO/KSFMO topmost surface layer, the oxygen vacancies (V_O) have two different environments due to different adjacent atoms, *i.e.*, Fe–V_O–Fe (Fig. 2b)

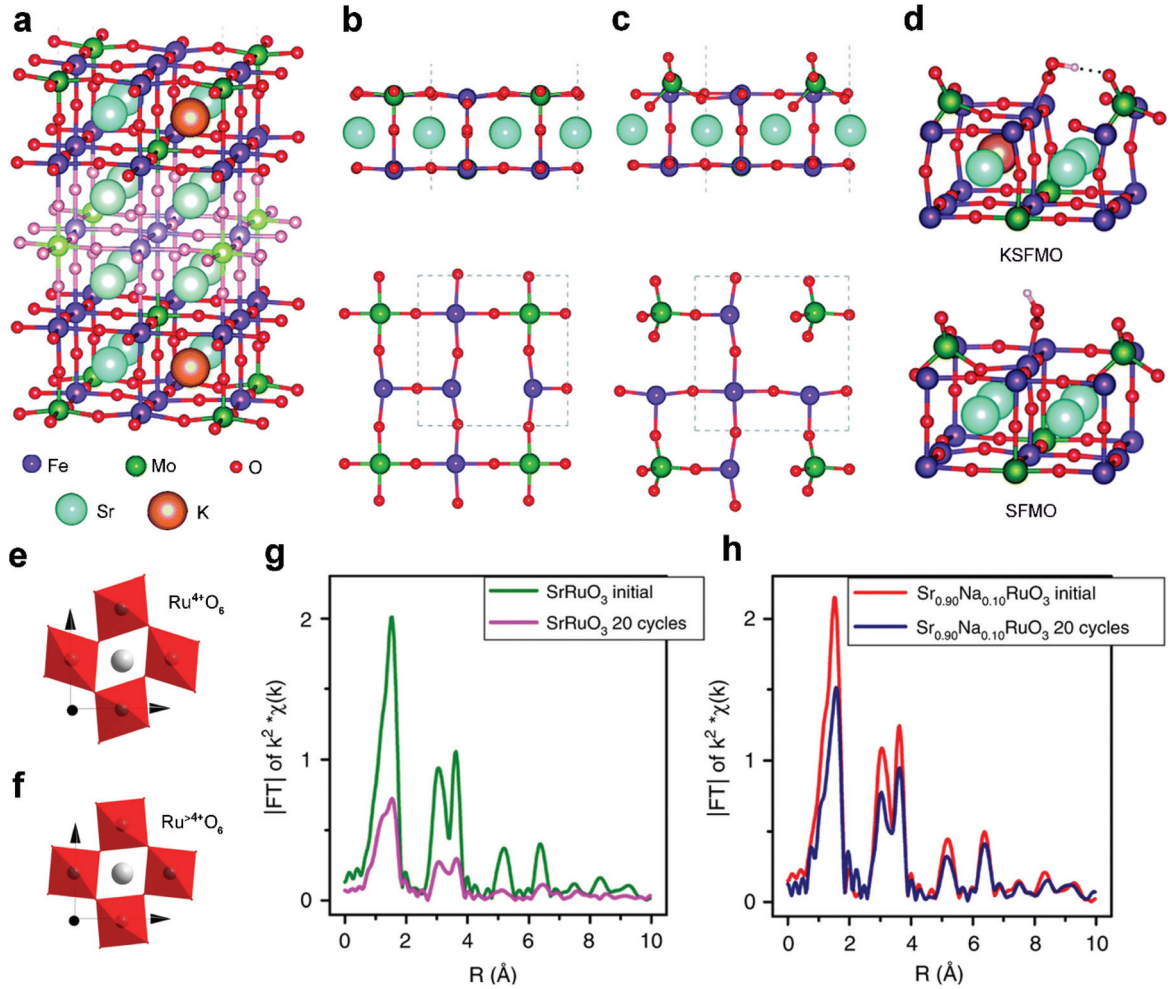

Fig. 2 (a) Structure of the 9-layer slab of KSFMO. Lateral and top views of the outermost layers after the formation of (b) Fe–V_O–Fe and (c) Mo–V_O–Fe. (d) Lateral view of the structures of the *OOH intermediates at Fe sites in KSFMO and in SFMO. Reproduced with permission from ref. 48. Copyright 2017, Royal Society of Chemistry. Schematic representation of octahedral distortion in (e) $SrRuO_3$ and (f) $Sr_{0.9}Na_{0.1}RuO_3$. Fourier transform from Ru K-edge EXAFS signals of (g) $SrRuO_3$ and (h) $Sr_{0.9}Na_{0.1}RuO_3$ before and after OER cycles. Reproduced with permission from ref. 49. Copyright 2019, Nature Publishing Group.

and Mo–V_O–Fe (Fig. 2c). When K atoms occupy A-site lattices, the V_O formation energies of Fe–V_O–Fe and Mo–V_O–Fe in KSFMO are lower than those in SFMO because of charge compensation effects.[68] Interestingly, KSFMO will suffer a peculiar surface reconstruction upon V_O formation along with Mo–V_O–Fe. The Mo atom and surrounding O atoms undergo a structural rearrangement from an unsaturated octahedron to a tetrahedron MoO_4 moiety, and Fe atoms become highly under-coordinated (Fig. 2c). H-Bonds are formed during the reconstruction of the MoO_4 tetrahedron to stabilize *OOH intermediates (Fig. 2d), which can accelerate the rate-determining step of the OER process. Meanwhile, the 3d orbital of the under-coordinated Fe cation, with a mixed Fe(III)/Fe(IV) character, has a strong overlap with the O 2p orbital, which is also beneficial for the ORR process.

The A-site doping of perovskite oxides with alkali metals also induces excellent cycling durability.[49] Pristine $SrRuO_3$ exhibits high specific OER activity but usually suffers from unsatisfactory durability, which is related to the distortion of $Ru^{4+}O_6$ octahedra in $SrRuO_3$ (Fig. 2e). Upon Na^+ doping, Ru^{4+} is slightly over-oxidized to $Ru^{>4+}$ because of charge compensation effects. Accordingly, the $Ru^{>4+}O_6$ octahedra are more regular in $Sr_{0.9}Na_{0.1}RuO_3$ (Fig. 2f) due to decreased Jahn–Teller effects. Thus, a severely decreased Ru–O signal is observed for the cycled $SrRuO_3$ (Fig. 2g), indicating severe structural degradation. Conversely, similar signals are displayed in fresh and cycled $Sr_{0.9}Na_{0.1}RuO_3$ (Fig. 2h), confirming the high structural stability. Na locally increases the oxidation state of Ru from +4 to +5 and weakens the too strong adsorption energies of the OER intermediates. If Ru^{5+} sites are instrumental for the development of $SrRuO_3$ perovskite oxide catalysts, other monovalent cations such as small radius Li^+ or large radius Cs^+ can be tested to ascertain whether they can also enhance the activity or the stability. This interesting

hypothesis would contribute to us for exploring other A-site alkali metal dopants.

2.2 A-site doping with alkaline-earth metals

In addition to alkali metal cations, bivalent alkaline-earth metal cations, such as Sr^{2+} and Ca^{2+}, have also been doped into the A-site of perovskite oxides to improve the electrocatalytic efficiency. The substitution of bivalent Sr^{2+} for trivalent A-site cations usually causes a charge imbalance throughout the perovskite oxides.[69] This imbalance leads to the generation of oxygen vacancies, the modulation of oxidation states of the B-site transition metals, and the regulation of surface

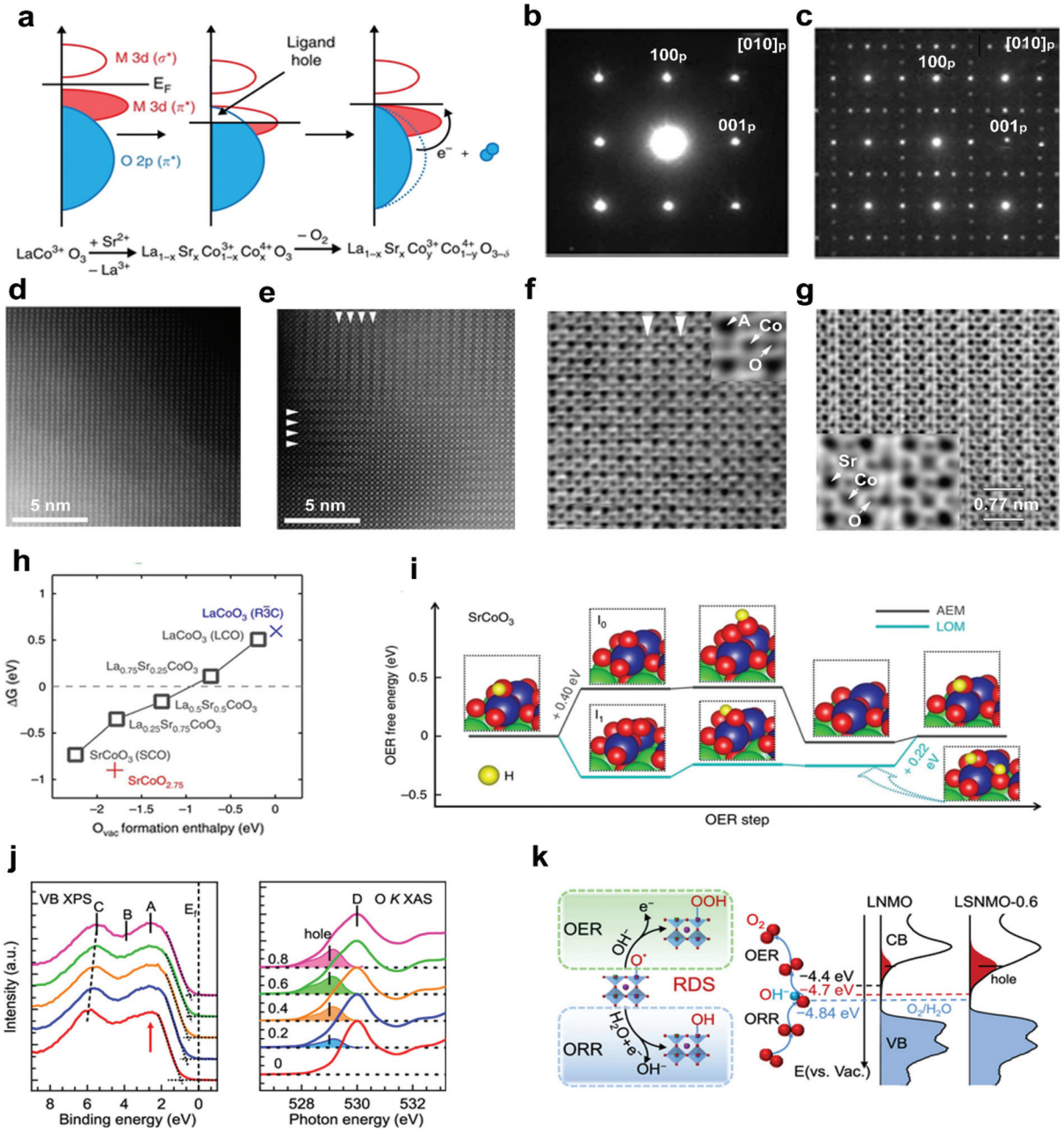

Fig. 3 (a) Schematic representation of the relationship between the oxygen vacancy concentration and Co–O bond covalency through Sr^{2+} doping. SAED patterns of (b) $La_{0.8}Sr_{0.2}CoO_3$ and (c) $SrCoO_3$. HAADF-STEM images of (d) $La_{0.8}Sr_{0.2}CoO_3$ and (e) $SrCoO_3$. ABF-STEM imaging of oxygen vacancy ordering in (f) $La_{0.2}Sr_{0.8}CoO_3$ and (g) $SrCoO_3$. (h) ΔG (free energy difference between the LOM and AEM) *versus* the oxygen vacancy formation energy in perovskite oxides with different Sr^{2+} concentrations. (i) The OER free energy changes of the LOM and AEM on $SrCoO_3$. Reproduced with permission from ref. 67. Copyright 2014, Nature Publishing Group. (j) X-ray photoemission spectroscopy valence band and O K-edge XAS spectra of LSNMO with different Sr^{2+}concentration. (k) Left panel: rate-determining step of the OER and the ORR. Right panel: schematics diagram for the electronic structure near the Fermi level. Reproduced with permission from ref. 70. Copyright 2021, American Chemical Society.

morphology.[67,70,71] Ca^{2+} doping can suppress surface segregation or induce a reformation into a stable structure, thereby yielding enhanced durability.[50,72]

In a recent study, aliovalent Sr^{2+} cations were used to substitute La^{3+} in $LaMO_3$ (M = Co, Fe, Ni, Mn), forming $La_{1-x}Sr_xCoO_{3-\delta}$,[67,71] $La_{1-x}Sr_xFeO_{3-\delta}$,[73] $La_{1-x}Sr_xNiO_{3-\delta}$,[51] and $La_{1-x}Sr_xMnO_{3-\delta}$,[74] as efficient OER and ORR catalysts. For example, Stevenson and co-workers reported that the oxidation states of Co and the band overlap of Co 3d/O 2p are increased through Sr^{2+} doping.[67] The formed ligand holes induce the release of lattice oxygen (Fig. 3a); therefore more oxygen vacancies will be created with the increased concentration of Sr^{2+} in the $La_{1-x}Sr_xCoO_3$ system. Compared with the crystal structures of low-level Sr^{2+} doped $La_{0.8}Sr_{0.2}CoO_3$ (Fig. 3b and d), obvious ordering of oxygen vacancies was observed in $SrCoO_3$ (Fig. 3c and e). The resulting layered ordered oxygen vacancies and atomic columns were directly observed in the high-level Sr^{2+} doped $La_{0.2}Sr_{0.8}CoO_3$ (Fig. 3f) and $SrCoO_3$ (Fig. 3g), due to the decreased formation energy of oxygen vacancies as the Sr^{2+} concentration increases (Fig. 3h). In addition, the oxygen evolution mechanism will transfer from the adsorbate evolution mechanism (AEM) to the lattice oxygen oxidation mechanism (LOM) with the increased Sr^{2+} concentration. The OER occurs *via* the AEM on $LaCoO_{3-\delta}$ and $La_{0.75}Sr_{0.25}CoO_{3-\delta}$, whereas on $La_{0.5}Sr_{0.5}CoO_{3-\delta}$ and $SrCoO_{3-\delta}$, it is mainly following the LOM mechanism (Fig. 3i).

The electronic structures of perovskite oxides can also be optimized by Sr^{2+} doping. It was found that when Sr^{2+} was doped into A sites, a shift of the whole valence band spectra towards the Fermi level (E_f) and excess hole states were observed in $La_{2-x}Sr_xNiMnO_6$ (LSNMO) (Fig. 3j).[70] Such electronic modulation enhances the hybridization of O 2p with Ni/Mn 3d, further reducing the charge transfer barrier and improving the intrinsic ORR and OER activities (Fig. 3k). The Sr^{2+} doping can also change the surface morphology due to the charge imbalance between Sr^{2+} and trivalent A-site cations. The unbalanced charge distribution may cause the local structural disorder in the [BO_6] octahedron, resulting in an increased specific surface area of $La_{1-x}Sr_xMnO_{3-\delta}$ and a newly formed amorphous layer in $La_{1-x}Sr_xCoO_{3-\delta}$ with electrocatalytic activities.[71,75] A series of grain boundaries would form as an internal interface when amorphous layers and crystal layers are in direct contact with each other. The grain boundaries are considered as distinctive platforms to exhibit new physical and chemical properties.[35] This would be interesting to explore the effect of dopant-induced grain boundaries on perovskite oxide electrocatalytic performance.

The durability of perovskite oxides can also be significantly enhanced after doping with alkaline-earth cations. Perovskite oxide catalysts usually suffer from degradations during long-term operations because of the adverse changes in their crystal-structures and unstable surface-properties.[76] For instance, a decrease in the activity of Ba-containing perovskite oxides is related to the surface degradation and Ba leaching.[77] Luo *et al.* stabilized the crystal structure of $PrBa_{0.85}Ca_{0.15}MnFeO_{5+\delta}$ (PBCMF) perovskite oxides by doping the A-site with Ca^{2+}.[50] Its pristine Ca-free counterpart, $PrBaMnFeO_{5+\delta}$ (PBMF), suffered from an obvious degradation after a 1000-cycle test in the water oxidation reactions. A ~10 nm Ba-rich shell was observed on the surface of degraded PBMF. In contrast, all the elements were uniformly distributed across the entire region in PBCMF. The calculation results reveal that a small amount of Ca-doping can increase the corrosion resistance in perovskite oxides, preventing surface degradation and Ba leaching. In addition, the Ca doping was reported to induce a structural transformation from layered perovskite oxides to cubic perovskite oxides with improved structural stability, which can deliver a durable OER performance.[77]

2.3 A-site doping with rare-earth metals

The A-site doping with rare-earth metals will result in a large cation-size mismatch and charge imbalance between rare-earth metal dopants and A-site metal cations, which can improve the conductivity, optimize the B-site electron states, and construct an active secondary phase for improved activities of perovskite oxides.[41,52]

Xie *et al.*[42] reported a combined method of Yb^{3+} doping and hydrogen treatment to improve the conductivity of $CaMnO_3$. The Yb^{3+} dopants with a higher valence compared to Ca^{2+} can help to inject electrons to the perovskite oxides,[78] introducing suitable oxygen vacancies for improved conductivity (Fig. 4a). Meanwhile, a similar radius between Yb^{3+} dopants and Ca^{2+} maintains the orthorhombic phase crystal structure of $Ca_{0.9}Yb_{0.1}MnO_{3-\delta}$ (Fig. 4b). The hydrogen treatment further improves the conductivity of $CaMnO_3$ by optimizing the e_g electron filling status (Fig. 4c), showing a linear increasing relationship (Fig. 4d). The introduction of Yb also caused the degeneration of Mn e_g orbitals into two sub-levels. The degeneration caused the elongation of Mn–O bonds owing to the Jahn–Teller effects (Fig. 4d). Such an elongation weakened the Mn–O covalent bond and facilitated the adsorption of oxygen intermediates. Therefore, significantly enhanced electrocatalytic activities were exhibited by the Yb-doped $Ca_{0.9}Yb_{0.1}MnO_{3-\delta}$.

In addition, rare-earth metal doping of the A-site in perovskite oxides can also contribute to the optimization of the electronic structure, leading to improved catalytic performance. Gao and co-workers reported an A-site doped $LaCoO_3$ with Ce^{3+} as a robust OER and ORR catalyst (Fig. 4e).[41] In pristine $LaCoO_3$, Co^{3+} is stabilized in the low-spin state (LS: $t_{2g}^6e_g^0$) and no obvious overlap is shown between the e_g band of Co and O 2p states near the Fermi level (Fig. 4f). Differently, in the Ce-$LaCoO_3$, the spin state of Co^{3+} transitions from the LS to the steady intermediate-spin state (IS: $t_{2g}^5e_g^1$). The downshifted e_g band toward the Fermi level enlarged the Co 3d/O 2p band overlap, resulting in efficient acceleration of electron transfer between active sites and oxygen intermediates (Fig. 4f). Accordingly, the electrons of Co^{3+} in 3d orbital transition from t_{2g} to e_g (Fig. 4g). Then, improved OER activities under alkaline conditions can be achieved through a steady σ interaction between the activated e_g orbitals of Co^{3+} and the O 2p orbitals of OH^- (Fig. 4h).[79]

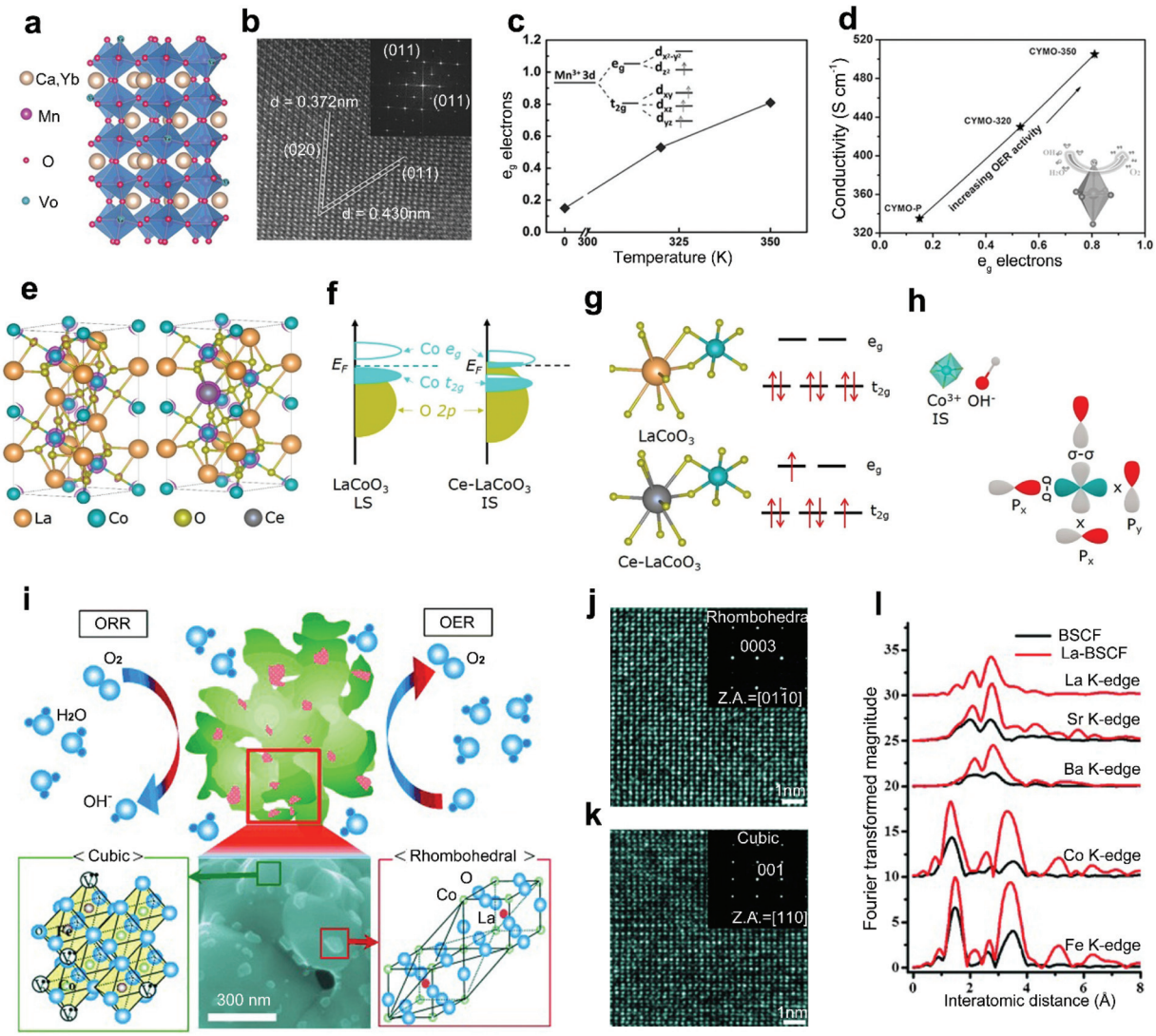

Fig. 4 (a) Crystal structure of $Ca_{0.9}Yb_{0.1}MnO_{3-\delta}$ with oxygen vacancies. (b) High-resolution TEM (HRTEM) image of $Ca_{0.9}Yb_{0.1}MnO_{3-\delta}$. (c) Hydrogen treatment temperature *versus* average e_g electrons. (d) The average e_g electrons *versus* electrical conductivity. Reproduced with permission from ref. 42. Copyright 2015, Wiley-VCH. (e) The crystal structure of $LaCoO_3$ and Ce-$LaCoO_3$. (f) Schematic representation of Co 3d–O 2p overlap for $LaCoO_3$ and Ce-$LaCoO_3$. (g) Schematic representation of the orbital splitting of Co 3d in $LaCoO_3$ and Ce-$LaCoO_3$. (h) Schematic representation of the interaction between the Co^{3+} and OH^- in Ce-$LaCoO_3$. Reproduced with permission from ref. 41. Copyright 2020, Elsevier B.V. (i) Schematic representation of La-BSCF perovskite oxide catalysts. HRTEM images and corresponding SAED patterns of (j) rhombohedral $LaCoO_3$ particles on the (k) cubic BSCF surface. (l) Radial distribution function for the all-atomic EXAFS spectra for BSCF and La-BSCF. Reproduced with permission from ref. 52. Copyright 2014, Wiley-VCH.

The surface morphology evolution, which would be induced by rare-earth metal doping in perovskite oxides, can also effectively affect the catalytic activities. Cho *et al.* reported a La-doped $La_{0.3}(Ba_{0.5}Sr_{0.5})_{0.7}Co_{0.8}Fe_{0.2}O_{3-\delta}$ (La-BSCF) as a promising bifunctional perovskite catalyst for the ORR and OER.[52] Compared with the conventional powder morphology of BSCF, La-BSCF shows a flower-shaped morphology with particles on surfaces (Fig. 4i). The dynamic microstructure phenomenon is attributed to the charge imbalance by aliovalent La^{3+} doping, forming rhombohedral $LaCoO_3$ (Fig. 4j) on the cubic BSCF surface (Fig. 4k). Additionally, the original Co–O bond in pristine BSCF is separated into two size-mismatched Co–O bonds (Fig. 4l). When compared with the BSCF, the La-BSCF with an excess active secondary phase provides more active sites for both the ORR and OER. For rhombohedral $LaCoO_3$ and cubic BSCF perovskite oxides, these two crystalline grains may form a grain boundary as an internal interface. This distinctive work provides an interesting idea to realize *in situ* formation of grain boundaries by heteroatom doping strategies.

3. B-site cation doping

In an ideal perovskite structure, transition metals occupying the $[BO_6]$ octahedron can directly affect the electrocatalytic perform-

ance of perovskite oxides.[80] To design high-performance perovskite oxide catalysts, it is rational to introduce heteroatoms into B-site lattices of perovskite oxides. To comprehensively elucidate the types of B-site dopants in perovskite oxides, noble metals (*e.g.*, Ir, Ru, Pt, Ag),[34,81–83] non-noble metals (*e.g.*, Mn, Fe, Co, Ni),[59,84–86] and non-metals (*e.g.*, P, Si)[58,87] will be introduced in this section.

3.1 B-site doping with noble metals

Doping highly active noble metals into the B-site of perovskite oxides is a typical strategy used to design highly efficient electrocatalysts, such as Ag-BSCF,[83] $La_{0.9}Fe_{0.92}Ru_{0.08}O_{3-\delta}$,[88] $Ba_{0.9}Sr_{0.1}Co_{0.8}Fe_{0.1}Ir_{0.1}O_{3-\delta}$,[89] and $LaCo_{1-x}Pt_xO_{3-\delta}$.[82] According to the work of Singhal *et al.*,[90] Ru-doped perovskite oxides show higher current densities and more capacitive behaviors than their Ru-free counterparts and RuO_2. This originates from the excellent ionic activities of Ru in doped perovskite oxides, which are even higher than that of ionic Ru in the benchmark RuO_2. Hereafter, the positive effects of B-site doping with noble metals mainly stem from modulated electronic structures of original catalytic sites and generated new heteroatom catalytic sites.

Zou and co-workers reported Ir doped $SrTiO_3$ (Ir-STO) with a remarkable OER activity in acidic media (Fig. 5a).[81] Pristine STO exhibits a negligible OER activity because the Ti 3d band is far from the Fermi level of STO (Fig. 5b). After the incorporation of Ir dopants, the electron density around Ti sites

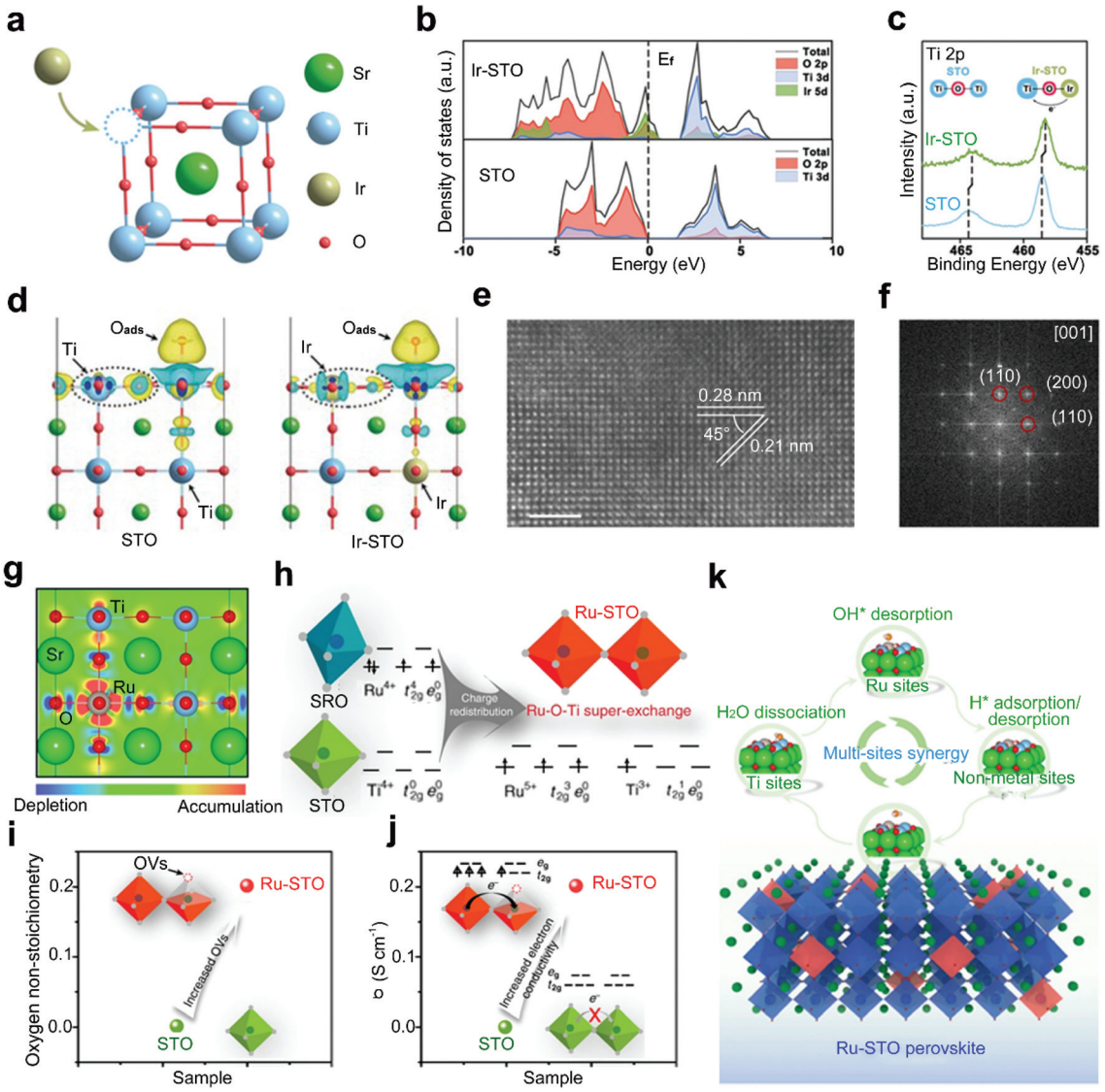

Fig. 5 (a) Schematic representation for the incorporation of Ir dopants in STO matrix. (b) DOS of Ir-STO and STO. (c) Ti 2p XPS spectra of Ir-STO and STO. (d) The charge density difference induced by oxygen adsorption on the Ti site in STO and Ir-STO. Reproduced with permission from ref. 81. Copyright 2019, Wiley-VCH. (e) HRTEM image and (f) corresponding fast Fourier transform (FFT) pattern of Ru-STO. (g) Schematic representation for top view of the charge distribution in Ru-STO. (h) Schematic representation of the super-exchange interaction in Ru-STO. (i) The oxygen non-stoichiometry and (j) electronic conductivity of STO and Ru-STO. (k) Schematic representation of the synergistic catalysis mechanism for an alkaline HER on Ru-STO. Reproduced with permission from ref. 34. Copyright 2020, Nature Publishing Group.

increases and the electrons are redistributed (Fig. 5c).[91] The density of states (DOS) of Ir-STO (Fig. 5b) also reveals an additional Ir electronic state crossing the Fermi level, and the Ti 3d band and O 2p band are closer to the Fermi level compared with STO. In this regard, the adsorption of oxygen intermediates on the Ti site is strengthened in the potential-determining step (Fig. 5d). This Ir doping strategy enables the possibility of designing high catalytic activity electrocatalysts for the OER under acid conditions, with a smaller amount of precious metals than their IrO_2 counterpart.

Dai and co-workers introduced a Ru-doped single-phase $SrTiO_3$, $SrTi_{0.7}Ru_{0.3}O_{3-\delta}$ (Ru-STO), with ultrafast HER performance in alkaline media (Fig. 5e and f).[34] The incorporation of Ru dopants into STO leads to a charge redistribution between the neighbouring Ti and Ru ions ($Ti^{4+} + Ru^{4+} \rightarrow Ti^{3+} + Ru^{5+}$) (Fig. 5g), resulting in an unusual super-exchange interaction between adjacent Ti^{3+} (with a $3d^1$ configuration) and doped Ru^{5+} (with a $4d^3$ configuration) (Fig. 5h).[43] In addition, oxygen vacancies are generated in the Ru-STO (Fig. 5i), which enhances the electrical conductivity (Fig. 5j) and contributes to exceptional catalytic activities. Density functional theory (DFT) calculations further reveal that the excellent activities are primarily attributed to a unique synergistic effect among the activated Ti sites, doped Ru sites and increased oxygen sites, which facilitate the water dissociation, enhance the OH* desorption, and promote the optimal H* adsorption and H_2 desorption, respectively (Fig. 5k).

Though B-site doping of perovskite oxides with noble metals is promising for achieving fast kinetics and high current density with a low overpotential, the large-scale commercial applications are restricted by the high cost and resource scarcity of the noble metals.[54] Besides, drastic structural instability during long-term operations has been observed, due to the dissolution of the formed noble metal oxides (RuO_x and IrO_x) on the surfaces of doped perovskite oxides.[49]

3.2 B-site doping with non-noble metals

Non-noble transition metals (*e.g.*, Fe, Co, Ni, Mn) have been intensively investigated as B-site dopants because of their common merits of low cost and Earth-abundance.[84–86] Some non-noble transition metals also have their specific merits. Mn-incorporated materials usually work well in the ORR,[52,92] Co/Ni-doped materials show high OER activities,[93–95] and Fe-based materials are relatively environmentally friendly.[96,97] Therefore, it is highly desirable to dope these non-noble transition metals into perovskite oxides for the development of large-scale energy production.

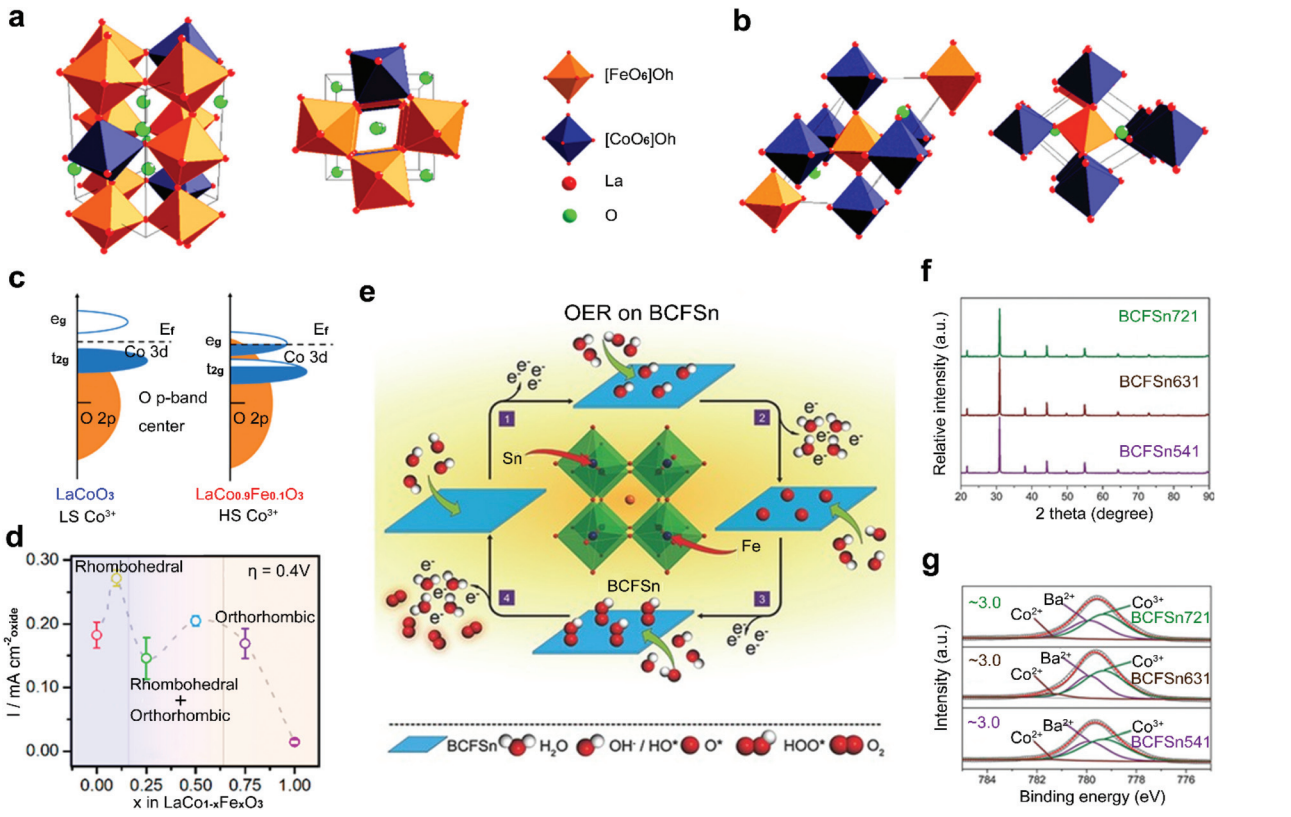

Fig. 6 Schematic representation for perovskite oxide structures with (a) distorted rhombohedral structure and (b) orthorhombic structure. (c) Schematic representation of Co 3d–O 2p overlap for $LaCoO_3$ and $LaCo_{0.9}Fe_{0.1}O_3$. (d) Specific current density and corresponding structure for $LaCo_{1-x}Fe_xO_3$ at an overpotential of 0.4 V *versus* RHE. Reproduced with permission from ref. 85. Copyright 2017, American Chemical Society. (e) Schematic representation of OER process of BCFSn perovskite oxides. (f) XRD patterns of BCFSn perovskite oxides. (g) High-resolution XPS spectra of Co $2p_{3/2}$ for BCFSn perovskite oxides. Reproduced with permission from ref. 103. Copyright 2016, Wiley-VCH.

Perovskite oxides are found to be more active toward the OER when a relatively small amount of Fe is doped into the B-site.[98,99] Xu and co-workers analysed the role of Fe-doping in perovskite oxide catalysts in the OER and found that the structure of $LaCoO_3$ is changed with the incorporated content of Fe. The $LaCo_{1-x}Fe_xO_3$ with a low concentration of doped Fe corresponds to a rhombohedral structure (Fig. 6a).[100] When the concentration of doped Fe increases, the $LaCo_{1-x}Fe_xO_3$ transitions from the rhombohedral phase to an orthorhombic phase (Fig. 6b). The phase change leads to the spin state transition of Co^{3+} from LS to HS and results in enhanced hybridization between Co 3d states and O 2p states (Fig. 6c). At an optimized concentration of doped Fe, remarkably enhanced OER activity is achieved (Fig. 6d). The doped Fe can also extend the potential range of thermodynamic metastability and improve the stability of the perovskite oxide structures through the formation of an oxy(hydroxide) layer on surfaces under OER conditions,[101] which is the actual active layer for the OER.[102]

Two kinds of transition metals can also be co-doped into the B-site of perovskite oxides. Shao *et al.* reported a co-doping strategy by introducing Fe and Sn into the B-site of inert $BaCoO_{3-\delta}$ to design highly active $BaCo_{0.9-x}Fe_xSn_{0.1}O_{3-\delta}$ (BCFSn) as OER catalysts (Fig. 6e).[103] The introduction of both Fe and Sn elements can not only optimize the OH^- adsorption capability, O_2 desorption capability, average metal–oxygen bond energy and electrical conductivity, but also stabilize the cubic-phase structure (Fig. 6f) and the oxidation state of surface Co atoms (Fig. 6g). Thus, a four-electron transfer pathway for the OER is greatly boosted in BCFSn. Some other co-doped perovskite oxides have also been developed, such as Co/Ni co-doped $Sr_2FeMoO_{6-\delta}$,[104] Cu/Co co-doped $LaMnO_{3-\delta}$,[105] and Cu/Fe co-doped $LaNiO_{3-\delta}$.[106] The optimized electronic structure of active sites and increased amount of oxygen vacancies are found in these co-doped perovskite oxides with improved catalytic activities.

3.3 B-site doping with non-metals

B-site doping of perovskite oxides with non-metal elements provides another attractive way to improve the electrocatalytic activities. Non-metal elemental dopants are inert by them-

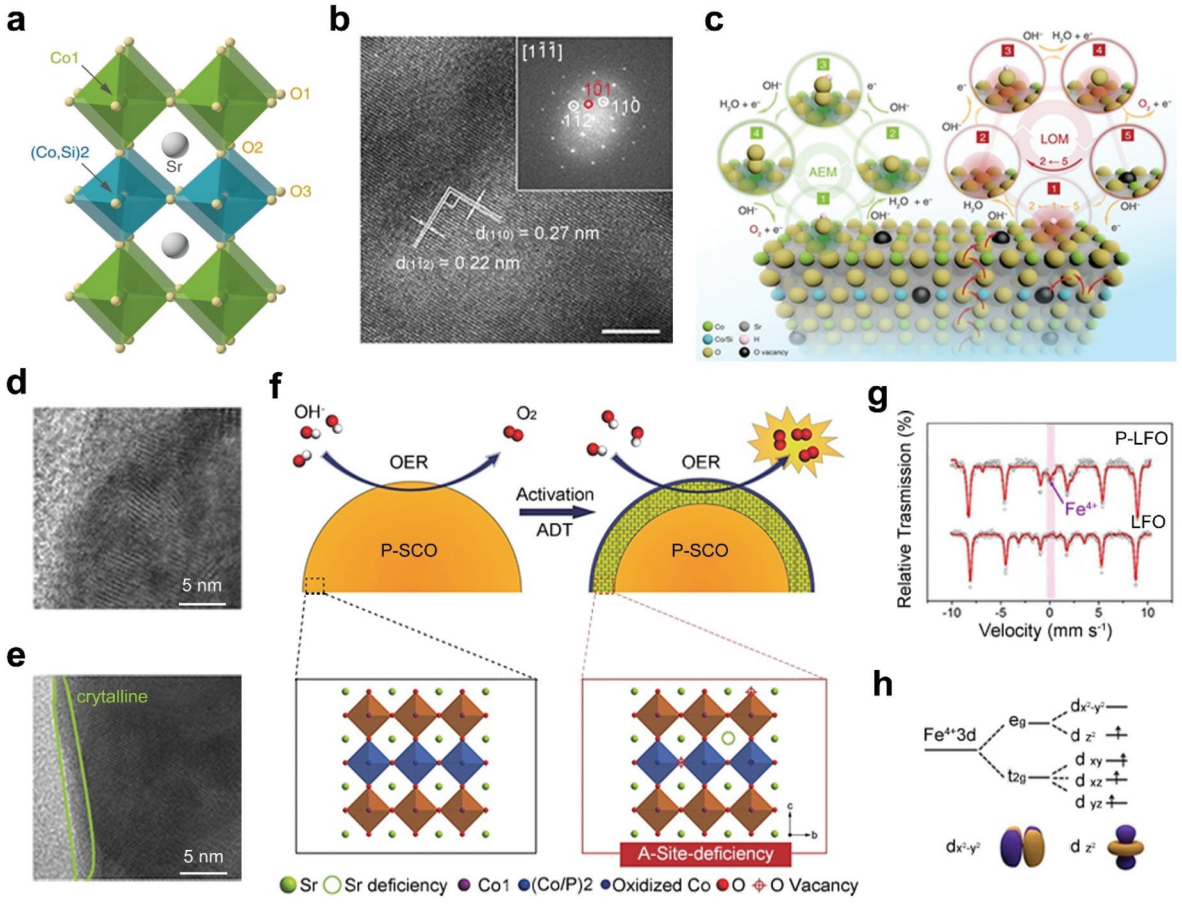

Fig. 7 (a) Schematic representation of the crystal structure of Si-SCO. (b) HRTEM image of Si-SCO and the corresponding FFT pattern. (c) Schematic representation of the AEM and LOM reaction pathways on Si-SCO. Reproduced with permission from ref. 58. Copyright 2020, Nature Publishing Group. (d) HRTEM images of surface regions of P-SCO (d) before and (e) after 1000 cycles. (f) Schematic representation of the main origin of the OER activation in the SCP sample. Reproduced with permission from ref. 57. Copyright 2016, Wiley-VCH. (g) Mössbauer spectrum of LFO and P-LFO. (h) Schematic representation of Fe 3d orbit degeneration. Reproduced with permission from ref. 87. Copyright 2018, Elsevier B.V.

selves towards electrocatalysis, such as silicon (Si) and phosphorus (P).[57,58,87,107] However, the non-metal elemental doping of perovskite oxides usually results in additional reaction pathways, favorable structural transitions, boosting electrical conductivities and optimized active sites, which are beneficial to efficient electrocatalysis.

Si doping can influence the catalytic performance of perovskite oxides through diverse ways, such as activation of additional reaction pathways, optimization of surface structures, and creation of oxygen vacancies. Shao's group introduced Si to the B-site of $SrCoO_3$ (Fig. 7a) to form a tetragonal-phase Si-$SrCoO_3$ (Si-SCO) (Fig. 7b).[58] The pH-dependence of the OER kinetics and almost unchanged e_g filling of Co in Si-SCO prove that the boosted electrocatalytic activities should be attributed to an activated LOM mechanism (Fig. 7c) instead of the AEM.[108] Besides, the increased pseudocapacitive behaviors of Si-SCO also indicate the involvement of lattice oxygen redox during the OER. The OER enhancement can also result from structural transition upon non-metal doping of perovskite oxides.[58] A Si-doped $SrFeO_{3-\delta}$ (Si-SFO) is designed and shows an approximately three-fold increase in OER activity relative to $SrFeO_{3-\delta}$.[107] This obviously enhanced OER activity can be ascribed to the structural transition from tetragonal to cubic phase originating from Si doping, accompanying the generation of abundant oxygen vacancies and further acceleration of charge transfer.

The introduction of P elements into perovskite oxides can affect the electrochemical surface areas and B-site electronic structures of perovskite oxides. For example, an increase in OER activities is observed for P-doped $SrCoO_3$ (P-SCO) after a 1000-cycle test.[57] This increase is due to the formation of an amorphous layer with a thickness of 1–2 nm on the surfaces of P-SCO during the durability tests (Fig. 7d and e). The surface amorphization, associated with the leaching of A-site Sr^{2+}, can lead to the exposure of active B sites and oxygen vacancies on the perovskite surface (Fig. 7f) and thus increase the electrochemical surface areas. Afterwards, Liu *et al.* found that compared with the pristine $LaFeO_{3-\delta}$ (LFO), P-doped $LaFeO_{3-\delta}$ (P-LFO) shows almost double times higher ORR activities under alkaline conditions.[87] Upon the incorporation of P, the valence states of partial Fe-sites increase from Fe^{3+} to Fe^{4+} (Fig. 7g). In particular, the generation of Fe^{4+} results in the degeneration of the Fe 3d orbital (Fig. 7h). With the coexistence of $Fe^{4+}/Fe^{3+}/Fe^{2+}$, the e_g electron filling is optimized

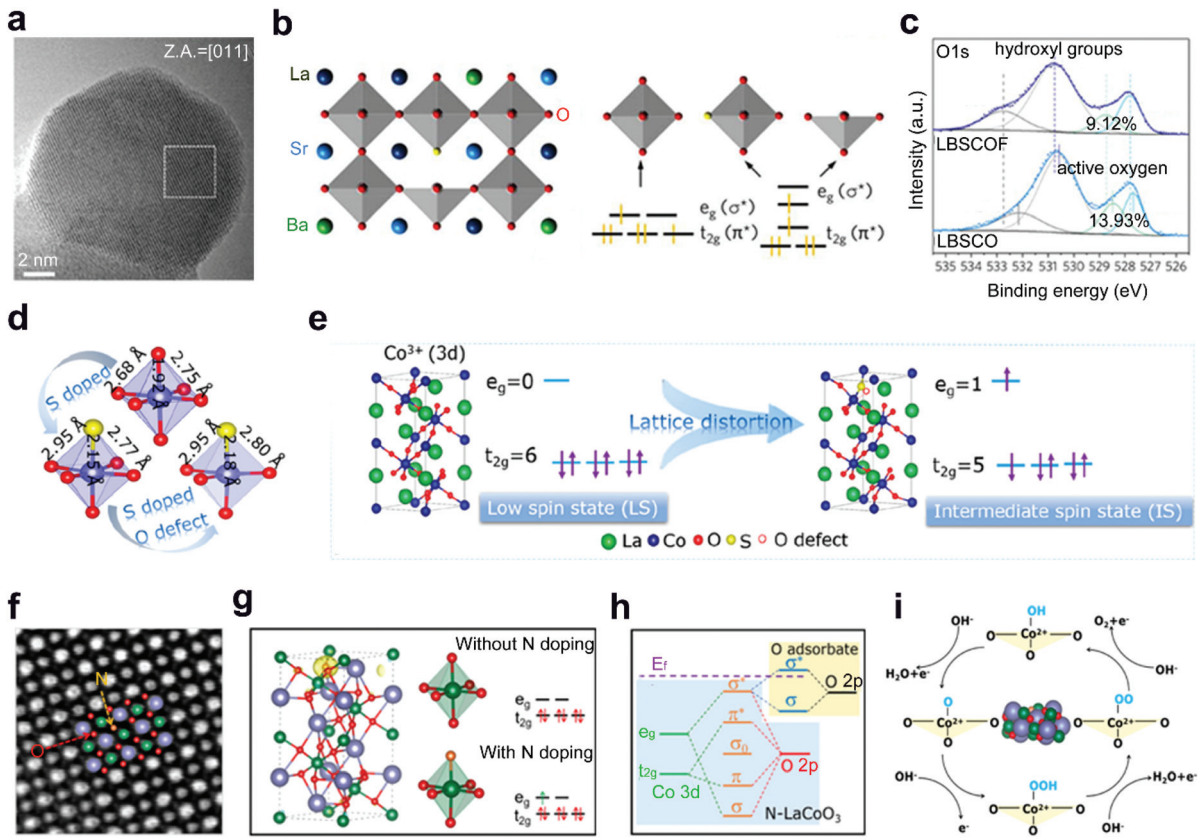

Fig. 8 (a) HRTEM image of LBSCOF. (b) Schematic representation of the perovskite oxide structure and featured [$CoO_{6-\delta}$] polyhedron. (c) XPS spectra of O 1s for LBSCOF and LBSCO. Reproduced with permission from ref. 60. Copyright 2018, Elsevier Inc. (d) Schematic representation for optimized atomic structures. (e) Schematic representation of the evolution of the IS state and the transition of electrons from t_{2g} to e_g orbital. Reproduced with permission from ref. 109. Copyright 2020, American Chemical Society. (f) ABF-STEM image of N-LCO. (g) Spin density distribution and electronic configuration of LCO and N-LCO. (h) Schematic representation of orbital bonding. (i) Illustration diagram of the four-step process of the OER. Reproduced with permission from ref. 62. Copyright 2021, American Chemical Society.

close to 1. What's more, the incorporation of P cations can also generate rich oxygen vacancies. With the optimized e_g orbital filling and abundant oxygen vacancies, P-LFO possesses enhanced ORR catalytic activity.

4. O-site anion doping

In addition to the above cation doping, replacement of partial oxygen anions in the perovskite oxides by other non-metal heteroatom anions has also been explored to improve the activities of perovskite oxides, such as F,[33,60] S,[61,109] N,[62] and Cl.[110] The introduction of anions with different electronegativities or valences into the perovskite matrix can decrease the formation energy of oxygen vacancies, modify the electronic state and induce surface structure transformation of perovskite, and therefore contribute to the manipulation of catalytic performance.

F is a widely used dopant to improve the electrocatalytic performance of perovskite oxides. Due to a less negative valence of −1 than −2 of O anions, the substitution of O with F induces a transformation from the $[CoO_6]$ octahedral structure to $[CoO_5F]$ and $[CoO_5]$ in cubic F-doped $La_{0.5}Ba_{0.25}Sr_{0.25}CoO_{3-\delta}$ and $La_{0.5}Ba_{0.25}Sr_{0.25}CoO_{3-\delta}F_{0.1}$ (LBSCOF) (Fig. 8a).[60] The formed octahedral $[CoO_5F]$ symmetry and square pyramidal $[CoO_5]$ symmetry lead to a reconfiguration of Co in the e_g and t_{2g} orbitals (Fig. 8b). Besides, owing to the larger electronegativity of F^- than that of O^{2-}, the coulombic force between B-site cations and O can be weakened upon F doping. Thus, a lower formation energy of the oxygen vacancy is needed in LBSCOF than that in pristine $La_{0.5}Ba_{0.25}Sr_{0.25}CoO_{3-\delta}$ (LBSCO). More content of active oxygen species is observed in LBSCOF than LBSCO (Fig. 8c). The opti-

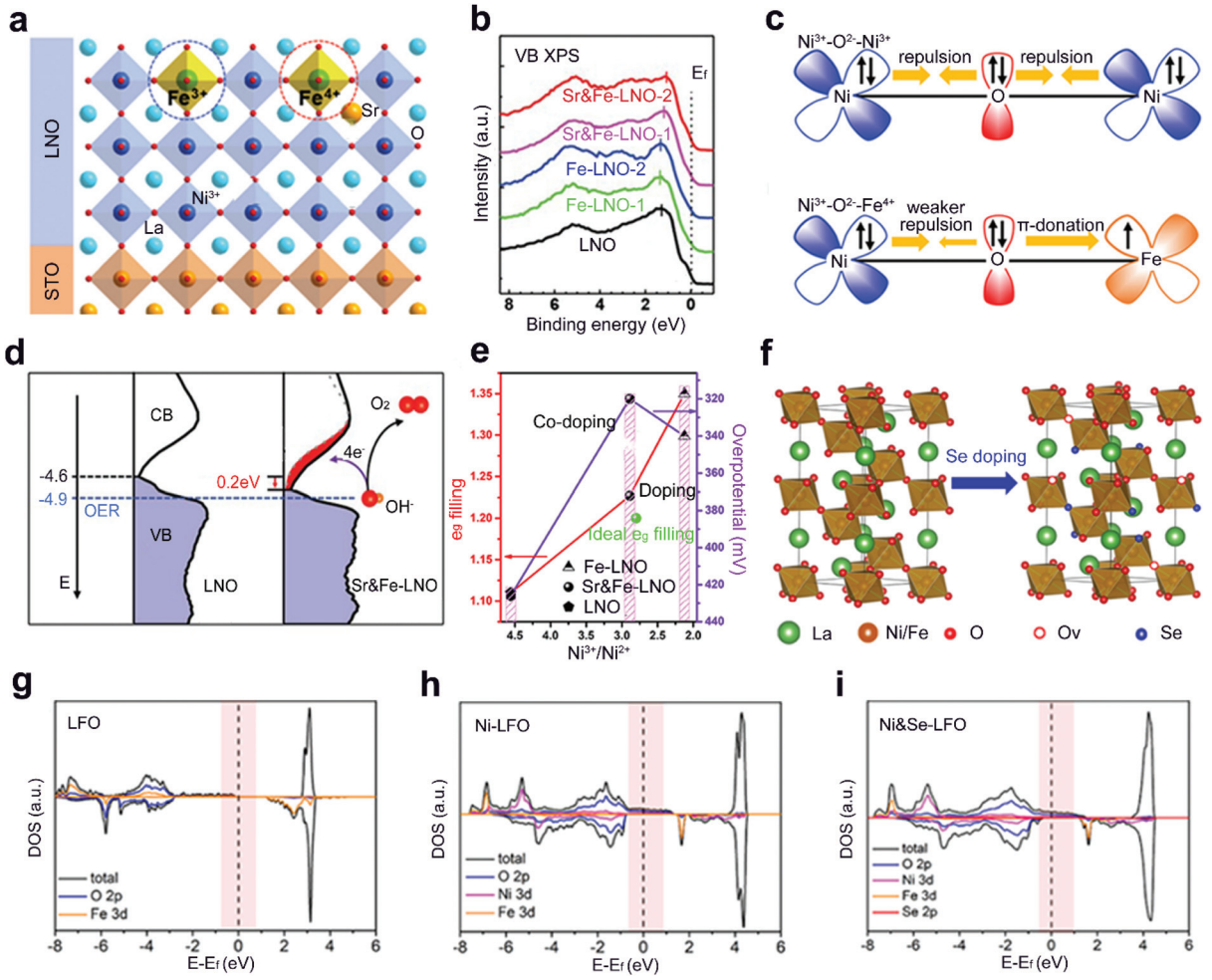

Fig. 9 (a) Schematic representation of epitaxial growth of Sr&Fe-LNO perovskite oxide thin films on a $SrTiO_3$ substrate. (b) XPS valence band spectrum and (c) schematic representation of the electronic coupling between the Ni^{3+} and Fe^{3+} in LNO and between the Ni^{3+} and Fe^{4+} in Sr&Fe-LNO, respectively. (d) The comparison of the occupied DOS (VB) and unoccupied DOS (CB) near E_f for LNO and Sr&Fe-LNO on an absolute energy scale. Reproduced with permission from ref. 64. Copyright 2021, Wiley-VCH. (e) The e_g orbital filling of different perovskite oxides and OER activity as a function of Ni^{3+}/Ni^{2+} rate. Reproduced with permission from ref. 63. Copyright 2019, Frontiers Media S.A. (f) Schematic representation of crystal structure of Ni-LFO and Ni&Se-LFO. DOS of (g) LFO, (h) Ni-LFO, and (i) Ni&Se-LFO, respectively. Reproduced with permission from ref. 47. Copyright 2020, American Chemical Society.

mized electronic orbital of Co and formed active oxygen species greatly promote the water-splitting reactions. As an element of the halogen group, Cl anions have the same −1 valence but lower electronegativity than F anions. Wang *et al.* experimentally investigated the role of Cl dopants. The enhanced OER activity of $LaFeO_{2.9-\delta}Cl_{0.1}$ was ascribed to the fact that the Cl dopants enriched abundant oxygen vacancies, increased the electrical conductivity and enhanced the Fe–O covalency.[110]

S is another efficient dopant for the O-site doping of perovskite oxides. S anions have the same −2 valence as O anions, but larger ionic radius than O anions. Therefore, the B–O bond lengths of [BO_6] octahedra are changed and oxygen vacancies are formed after doping S into the O-site. These phenomena are observed in a recently reported S-doped $LaCoO_3$ (S-LCO).[109] During the *in situ* vapor–solid reaction process, the sulfur atoms react with $LaCoO_3$ perovskite oxides and are reduced into sulfur anions. The sulfur anions are anchored on the O sites and a distorted [BO_6] octahedral structure is formed (Fig. 8d). The distorted structure induces the spin state transition of Co from low spin to intermediate spin in S-LCO (Fig. 8e). Compared with pristine LCO, S-LCO shows greatly improved activities for both the OER and ORR under alkaline conditions. The influences of S dopants during the electrocatalytic process are also investigated by DFT calculations. Theoretical simulation reveals an elongated O═O double bond in S doped perovskite oxides during the ORR process.[61] The easier O_2 cleavage indicates that S doping can endow perovskite oxides with an optimal electronic structure and surface adsorption feature for ORR catalysis.

With a low electronegativity and a high level of the 2p orbital, N atoms can exchange electrons in 2p orbitals with 3d orbitals of B-site active cations.[111] Recently, Gao and co-workers reported an N-doped $LaCoO_3$ (N-LCO) with enhanced oxygen catalytic activities (Fig. 8f).[62] In typical $LaCoO_3$, the Co cations show a low spin state with e_g occupancy of ~0. In contrast, in the N-LCO, N provides Co with an additional electron through the N–Co bond, resulting in a moderate e_g occupancy of ~1 for the Co cations (Fig. 8g). Then, the interaction between the 3d orbital of Co^{3+} and the 2p orbital of surface-adsorbed O intermediates is promoted (Fig. 8h). Eventually, a four-step process of the OER is greatly accelerated (Fig. 8i).

5. Dual-site doping

Although single-site doping of heteroatoms into ABO_3 perovskite oxides has been intensively studied, the optimized performance is still somehow far from satisfaction. Recently, a dual-site doping strategy has been explored by doping diverse heteroatom dopants into A and B sites or B and O sites of perovskite oxides. A synergistic promotion is supposed to be achieved among multi-active sites induced by dual-site doping.[47,63,64]

Zhang *et al.* doped Sr and Fe heteroatoms into A and B sites of $LaNiO_3$ (LNO), respectively (Fig. 9a).[64] Single-site doping of

Table 1 Catalytic performance comparisons of doped and pristine perovskite oxide catalysts

Composition engineering	Dopants	Catalysts Doped/pristine materials	Catalytic performance HER[a]	OER[b]	ORR[c]	Ref.
A site doping	Na	$Sr_{0.95}Na_{0.05}RuO_3/SrRuO_3$		0.16/0.19		49
	Sr	$La_{0.8}Sr_{0.2}CoO_3/LaCoO_3$		0.41/0.44		67
	Ce	Ce-$LaCoO_3/LaCoO_3$		0.41/0.65	0.68/0.45	41
	La	$La_{0.3}(Ba_{0.5}Sr_{0.5})_{0.7}Co_{0.8}Fe_{0.2}O_3/Ba_{0.5}Sr_{0.5}Co_{0.8}Fe_{0.2}O_3$		0.32/0.44		52
	Sr	$La_{0.2}Sr_{0.8}Co_{0.8}Fe_{0.2}O_{3-\delta}/LaCo_{0.8}Fe_{0.2}O_{3-\delta}$		0.45/0.56		71
	Sr	$La_{0.5}Sr_{0.5}FeO_{3-\delta}/LaFeO_3$		0.24/0.35		73
B site doping	Ti	$SrTi_{0.7}Ru_{0.3}O_{3-\delta}/SrRuO_{3-\delta}$	0.05/0.09			33
	Ir	$SrTi_{0.67}Ir_{0.33}O_3/SrTiO_3$		0.24/0.32		81
	Pt	$LaCo_{0.94}Pt_{0.06}O_{3-\delta}/LaCoO_{3-\delta}$	0.29/0.44	0.454/0.541		82
	Ag	Ag-$Ba_{0.5}Sr_{0.5}Co_{0.8}Fe_{0.2}O_{3-\delta}/Ba_{0.5}Sr_{0.5}Co_{0.8}Fe_{0.2}O_{3-\delta}$		0.44/0.51		83
	Si	Si-$SrCoO_{3-\delta}/SrCoO_{3-\delta}$		0.417/0.488		58
	Co	$LaFe_{0.8}Co_{0.2}O_3/LaFeO_3$		0.34/0.36		59
	Fe	$La_{0.58}Sr_{0.4}Co_{0.8}Fe_{0.2}O_3/La_{0.58}Sr_{0.4}CoO_3$		0.422/0.490		92
	Ru	$SrCo_{0.9}Ru_{0.1}O_{3-\delta}/SrCoO_{3-\delta}$		0.36/0.44		43
	Sn/Fe	$BaCo_{0.7}Fe_{0.2}Sn_{0.1}O_{3-\delta}/BaCoO_{3-\delta}$		0.42/0.45		103
O site doping	S	S doped $LaCoO_3/LaCoO_3$		0.364/0.473		109
	Cl	$LaFeO_{2.9-\delta}Cl_{0.1}/LaFeO_3$		0.47/0.51		110
	F	F-$Ba_{0.5}Sr_{0.5}Co_{0.8}Fe_{0.2}O_{3-\delta}/Ba_{0.5}Sr_{0.5}Co_{0.8}Fe_{0.2}O_{3-\delta}$		0.28/0.34		33
	F	$La_{0.5}Ba_{0.25}Sr_{0.25}CoO_{2.9-\delta}F_{0.1}/La_{0.5}Ba_{0.25}Sr_{0.25}CoO_{3-\delta}$	0.17/0.22	0.39/0.43		60
	S	S doped $CaMnO_3/CaMnO_3$		0.47/0.62	0.72/0.68	61
	N	N doped $LaCoO_3/LaCoO_3$		0.37/0.57	0.63/0.62	62
Dual site doping	Se, Ni	Se, Ni doped $LaFeO_3/LaFeO_3$		0.307/0.330		47
	Sr, Fe	$La_{0.4}Sr_{0.6}Ni_{0.5}Fe_{0.5}O_3/LaNiO_3$		0.320/0.473		63
	Sr, Fe	Sr, Fe doped $LaNiO_3/LaNiO_3$		0.33/0.49		64

[a] The overpotential at a current density of 10 mA cm^{-2} (V *vs.* RHE). [b] The overpotential at a current density of 10 mA cm^{-2} (V *vs.* RHE). [c] Half-wave potential (V *vs.* RHE).

LNO with Fe (Fe-LNO) only shows a Fe^{3+} oxidation state with a shift of the whole valence band (VB) photoemission spectrum of Fe-LNO away from E_f (Fig. 9b). However, the Sr and Fe dual-site doped LNO (Sr&Fe-LNO) shows a promoted Fe state from +3 to +4. The activated Fe^{4+} states induce an inverse shift of the whole VB spectrum back close to E_f (Fig. 9b). The presence of Fe^{4+} can also reduce the electron–electron repulsion from bridging O (Fig. 9c) and facilitate the generation of active Ni^{4+} states. Besides, a reduced energy barrier of electron transfer is achieved for the Sr&Fe-LNO compared with LNO (Fig. 9d). Consequently, a six times higher current density is obtained for the Sr&Fe-LNO than that of LNO and Fe-LNO. In another report, by regulating the proportion of Sr and Fe nitrate precursors, an optimal e_g-filling value of 1.2 is achieved through the dual-site doping with Sr and Fe (Fig. 9e).[63]

Dual-site doped $LaFeO_3$ with Ni and Se into B and O sites, respectively, is explored as a robust OER catalyst (Fig. 9f).[47] The adsorption energies of oxygenated species on Fe sites are stronger than those of Ni sites.[112] The substitution of the B-site Fe by adding different amounts of nickel salts into precursor solutions can optimize the adsorption of oxygen intermediates during the OER process. Furthermore, a mixture of Se powder and Ni single-site doped LFO (Ni-LFO) is annealed under an argon atmosphere. Se atoms are doped into O sites and lead to the formation of tremendous oxygen vacancies. The electron-occupied states crossing the Fermi level are increased in Ni and Se dual-site doped LFO (Ni&Se-LFO) compared to Ni-LFO and LFO (Fig. 9g–i). Finally, both experimental results and theoretical calculations demonstrate that Ni&Se-LFO shows superior OER catalytic activities to single-doped Ni-LFO and LFO.

6. Conclusion and perspective

This review summarizes the recent advances in the heteroatom doping of perovskite oxides. The catalytic performances of current doped perovskite oxide catalysts are listed in Table 1. The types of doping were classified in terms of the categories of the doping sites in ABO_3-type perovskite oxide structures, including A-site doping, B-site doping, O-site doping, and dual-site doping. Based on these doping strategies, the electrocatalytic activities of perovskite oxides can be effectively enhanced by the optimization of active site states, introduction of oxygen vacancies, regulation of surface morphologies, and surface reconstruction. Nevertheless, there are also many challenges that deserve further investigation.

Most of the present research studies focus on single-site doping of perovskite oxides with heteroatoms. Compared with single-site doping, dual-site doping is supposed to show higher energy-efficiency for perovskite oxides.[47,63,64] Available examples mentioned above have demonstrated that dual-site doping could introduce more remarkable influences on the electrocatalytic behaviors of perovskite oxides, thus worthy of our in-depth study. Current research studies have focused on doping different types of heteroatoms into multiple sites. However, there are enormous possible combinations of heteroatom dopants in perovskite oxide materials, which intensively hinder our efficient screening in the search for a combination with optimal catalytic properties. Thus, for a dual-site doping strategy, how to select the optimal heteroatom dopants remains a huge challenge. Recently, S has been doped into both B sites and O sites of perovskite oxides simultaneously, due to its relatively moderate electronegativity.[57,61] It is highly possible that some other non-metal elements with similar electronegativity could also function as both an electron acceptor and an electron donor, showing great potential of multi-site dopants for next-generation doping strategies.

While searching for optimal doping strategies, advanced *in situ* techniques should be considered to clarify the dynamic variation of dopant precursors during the doping process and real-time interaction between the doped heteroatoms and active sites during catalytic reactions. For example, *in situ* scanning transmission electron microscopy (STEM) characterization can facilitate our accurate determination of the locations of heteroatoms and record of atomic displacements of active sites.[35] Operando X-ray absorption spectral (XAS) measurements can help to understand the functional role of doped heteroatoms in perovskite oxides during the catalytic reactions.[101] *In situ* Raman technology can capture the dynamic surface reconstruction and facilitate our understanding of the surface catalytic mechanism during the evolution of the active phase.[113] Currently, Bao's group discovered the reversible exsolution and dissolution of metal nanoparticles in Co-doped $Sr_2Fe_{1.5}Mo_{0.5}O_{6-\delta}$ (Co-SFMC) perovskite oxides using advanced *in situ* techniques.[114] *In situ* XRD and STEM revealed that the doped Co was exsolved from the parent perovskite and facilitated the generation of CoFe alloy nanoparticles on the surface of Co-SFMC, leading to enhanced CO_2 electrolysis performance. These *operando* techniques visually demonstrate the structural evolution of electrocatalysts and provide us with more detailed research to understand the specific behavior of heteroatoms for catalyst synthesis and reaction processes.

The current research studies of doped perovskite oxide electrocatalysts are mainly focused on the HER, OER, and ORR. Currently, perovskite oxides have been demonstrated with activities toward the NRR under ambient conditions.[30,115] The activities are mainly attributed to the favourable merits produced by the oxygen vacancies, which could have originated from heteroatom doping. Indeed, Bi's group improved the NRR catalytic performance of heteroatom-doped perovskite oxides.[116] They found that A-site Sr doping can create abundant oxygen vacancies in Sr-doped LFO ($La_{0.5}Sr_{0.5}FeO_{3-\delta}$). The enriched oxygen vacancies weaken the N≡N triple bonds and accelerate the formation of N–H bonds. Considering the high composition tunability of perovskite oxides and various types of heteroatom dopants, we anticipate that perovskite oxide catalysts doped with specific and optimized heteroatoms may be applied to other catalytic fields.

Overall, perovskite oxide-based electrocatalysts will indeed have a promising outlook in the electrocatalytic field, owing to

their multiple advantages of Earth abundance, low cost, structural diversity and high efficiency. With the gradually optimized synthetic strategies and advanced *in situ* techniques, the role of heteroatom dopants will be further understood at the atomic level. The heteroatom doping strategy could pave the way for the development of practical perovskite oxide catalysts for widespread applications in energy-related catalysis fields.

Conflicts of interest

There are no conflicts to declare.

Acknowledgements

This work was supported by the National Natural Science Foundation of China (52125202, 22179062, 51902161, U2004209, and 21908110). J. S. thanks the Natural Science Foundation of Jiangsu Province (BK20190479). L. X. acknowledges the support from the China Postdoctoral Science Foundation (2020M681613 and 2021T140326).

References

1 L. C. Seitz, C. F. Dickens, K. Nishio, Y. Hikita, J. Montoya, A. Doyle, C. Kirk, A. Vojvodic, H. Y. Hwang, J. K. Norskov and T. F. Jaramillo, *Science*, 2016, **353**, 1011–1014.
2 H. N. Nong, L. J. Falling, A. Bergmann, M. Klingenhof, H. P. Tran, C. Spori, R. Mom, J. Timoshenko, G. Zichittella, A. Knop-Gericke, S. Piccinin, J. Perez-Ramirez, B. R. Cuenya, R. Schlogl, P. Strasser, D. Teschner and T. E. Jones, *Nature*, 2020, **587**, 408–413.
3 F. Pelayo García de Arquer, C. T. Dinh, A. Ozden, J. Wicks, C. McCallum, A. R. Kirmani, D. H. Nam, C. Gabardo, A. Seifitokaldani, X. Wang, Y. C. Li, F. Li, J. Edwards, L. J. Richter, S. J. Thorpe, D. Sinton and E. H. Sargent, *Science*, 2020, **367**, 661–666.
4 B. Sun, P. Xiong, U. Maitra, D. Langsdorf, K. Yan, C. Wang, J. Janek, D. Schroder and G. Wang, *Adv. Mater.*, 2020, **32**, 1903891.
5 P. Xiong, R. Ma, G. Wang and T. Sasaki, *Energy Storage Mater.*, 2019, **19**, 281–298.
6 J. Hwang, R. R. Rao, L. Giordano, Y. Katayama, Y. Yu and Y. Shao-Horn, *Science*, 2017, **358**, 751–756.
7 C. Guo, P. He, R. Cui, Q. Shen, N. Yang and G. Zhao, *Adv. Energy Mater.*, 2019, **9**, 1900364.
8 X. Huang, Q. Shen, J. Liu, N. Yang and G. Zhao, *Energy Environ. Sci.*, 2016, **9**, 3161.
9 Z. Zhou, Z. Wu, Q. Xu and G. Zhao, *J. Mater. Chem. A*, 2017, **5**, 25450.
10 D. J. Kubicki, S. D. Stranks, C. P. Grey and L. Emsley, *Nat. Rev. Chem.*, 2021, **5**, 624.
11 P. Xiong, Y. Wu, Y. Liu, R. Ma, T. Sasaki, X. Wang and J. Zhu, *Energy Environ. Sci.*, 2020, **13**, 4834–4853.
12 Z. Zhou, Y.-N. Xie, W. Zhu, H. Zhao, N. Yang and G. Zhao, *Appl. Catal., B*, 2021, **286**, 119868.
13 M. Zhang, G. Jeerh, P. Zou, R. Lan, M. Wang, H. Wang and S. Tao, *Mater. Today*, 2021, DOI: 10.1016/j.mattod.2021.05.004.
14 Y. R. Zheng, P. Wu, M. R. Gao, X. L. Zhang, F. Y. Gao, H. X. Ju, R. Wu, Q. Gao, R. You, W. X. Huang, S. J. Liu, S. W. Hu, J. Zhu, Z. Li and S. H. Yu, *Nat. Commun.*, 2018, **9**, 2533.
15 H. Huang, M. Yan, C. Yang, H. He, Q. Jiang, L. Yang, Z. Lu, Z. Sun, X. Xu, Y. Bando and Y. Yamauchi, *Adv. Mater.*, 2019, **31**, 1903415.
16 Q. Yao, B. Huang, Y. Xu, L. Li, Q. Shao and X. Huang, *Nano Energy*, 2021, **84**, 105909.
17 C. Cui, R. Cheng, C. Zhang and X. Wang, *Chin. Chem. Lett.*, 2020, **31**, 988–991.
18 P. Xiong, F. Zhang, X. Zhang, S. Wang, H. Liu, B. Sun, J. Zhang, Y. Sun, R. Ma, Y. Bando, C. Zhou, Z. Liu, T. Sasaki and G. Wang, *Nat. Commun.*, 2020, **11**, 3297.
19 P. Xiong, R. Ma, N. Sakai and T. Sasaki, *ACS Nano*, 2018, **12**, 1768–1777.
20 P. Xiong, X. Zhang, F. Zhang, D. Yi, J. Zhang, B. Sun, H. Tian, D. Shanmukaraj, T. Rojo, M. Armand, R. Ma, T. Sasaki and G. Wang, *ACS Nano*, 2018, **12**, 12337–12346.
21 S. Wang, P. Xiong, X. Guo, J. Zhang, X. Gao, F. Zhang, X. Tang, P. H. L. Notten and G. Wang, *Adv. Funct. Mater.*, 2020, **30**, 2001588.
22 S. Wang, P. Xiong, J. Zhang and G. Wang, *Energy Storage Mater.*, 2020, **29**, 310–331.
23 L. Peng, P. Xiong, L. Ma, Y. Yuan, Y. Zhu, D. Chen, X. Luo, J. Lu, K. Amine and G. Yu, *Nat. Commun.*, 2017, **8**, 15139.
24 K. Jiang, P. Xiong, J. Ji, J. Zhu, R. Ma, T. Sasaki and F. Geng, *Acc. Chem. Res.*, 2020, **53**, 2443–2455.
25 W.-J. Yin, B. Weng, J. Ge, Q. Sun, Z. Li and Y. Yan, *Energy Environ. Sci.*, 2019, **12**, 442–462.
26 H. J. Song, H. Yoon, B. Ju and D. W. Kim, *Adv. Energy Mater.*, 2020, **11**, 2002428.
27 C. Sun, J. A. Alonso and J. Bian, *Adv. Energy Mater.*, 2020, **11**, 2000459.
28 L. Wang, K. A. Stoerzinger, L. Chang, J. Zhao, Y. Li, C. S. Tang, X. Yin, M. E. Bowden, Z. Yang, H. Guo, L. You, R. Guo, J. Wang, K. Ibrahim, J. Chen, A. Rusydi, J. Wang, S. A. Chambers and Y. Du, *Adv. Funct. Mater.*, 2018, **28**, 1803712.
29 R. P. Singh, P. Arora, S. Nellaiappan, C. Shivakumara, S. Irusta, M. Paliwal and S. Sharma, *Electrochim. Acta*, 2019, **326**, 134952.
30 S. Zhang, G. Duan, L. Qiao, Y. Tang, Y. Chen, Y. Sun, P. Wan and S. Zhang, *Ind. Eng. Chem. Res.*, 2019, **58**, 8935–8939.
31 J. Suntivich, K. J. May, H. A. Gasteiger, J. B. Goodenough and Y. Shao-Horn, *Science*, 2011, **334**, 1383–1385.
32 D. Yan, Y. Li, J. Huo, R. Chen, L. Dai and S. Wang, *Adv. Mater.*, 2017, **27**, 1606459.

33 J. Xiong, H. Zhong, J. Li, X. Zhang, J. Shi, W. Cai, K. Qu, C. Zhu, Z. Yang, S. P. Beckman and H. Cheng, *Appl. Catal., B*, 2019, **256**, 117817.
34 J. Dai, Y. Zhu, H. A. Tahini, Q. Lin, Y. Chen, D. Guan, C. Zhou, Z. Hu, H. J. Lin, T. S. Chan, C. T. Chen, S. C. Smith, H. Wang, W. Zhou and Z. Shao, *Nat. Commun.*, 2020, **11**, 5657.
35 Y. Heo, S. Choi, J. Bak, H. S. Kim, H. B. Bae and S. Y. Chung, *Adv. Energy Mater.*, 2018, **8**, 1802481.
36 J. R. Petrie, H. Jeen, S. C. Barron, T. L. Meyer and H. N. Lee, *J. Am. Chem. Soc.*, 2016, **138**, 7252–7255.
37 M. J. Choi, T. L. Kim, J. K. Kim, T. H. Lee, S. A. Lee, C. Kim, K. Hong, C. W. Bark, K. T. Ko and H. W. Jang, *Nano Lett.*, 2020, **20**, 8040–8045.
38 Y. Zhu, W. Zhou, J. Yu, Y. Chen, M. Liu and Z. Shao, *Chem. Mater.*, 2016, **28**, 1691–1697.
39 J. I. Jung, H. Y. Jeong, M. G. Kim, G. Nam, J. Park and J. Cho, *Adv. Mater.*, 2015, **27**, 266–271.
40 Y. Chen, H. Li, J. Wang, Y. Du, S. Xi, Y. Sun, M. Sherburne, J. W. Ager III, A. C. Fisher and Z. J. Xu, *Nat. Commun.*, 2019, **10**, 572.
41 J. Qian, T. Wang, Z. Zhang, Y. Liu, J. Li and D. Gao, *Nano Energy*, 2020, **74**, 104948.
42 Y. Guo, Y. Tong, P. Chen, K. Xu, J. Zhao, Y. Lin, W. Chu, Z. Peng, C. Wu and Y. Xie, *Adv. Mater.*, 2015, **27**, 5989–5994.
43 J. Dai, Y. Zhu, Y. Yin, H. A. Tahini, D. Guan, F. Dong, Q. Lu, S. C. Smith, X. Zhang, H. Wang, W. Zhou and Z. Shao, *Small*, 2019, **15**, 1903120.
44 Y. R. Sun, X. Zhang, L. G. Wang, Z. K. Liu, N. Kang, N. Zhou, W. L. You, J. Li and X. F. Yu, *Chem. Eng. J.*, 2021, **421**, 129698.
45 Y. Zhu, X. Liu, S. Jin, H. Chen, W. Lee, M. Liu and Y. Chen, *J. Mater. Chem. A*, 2019, **7**, 5875–5897.
46 J. Zhang, Y. Cui, L. Jia, B. He, K. Zhang and L. Zhao, *Int. J. Hydrogen Energy*, 2019, **44**, 24077–24085.
47 Z. Li, K. H. Xue, J. Wang, J. G. Li, X. Ao, H. Sun, X. Song, W. Lei, Y. Cao and C. Wang, *ACS Appl. Mater. Interfaces*, 2020, **12**, 41259–41268.
48 A. B. Muñoz-García and M. Pavone, *J. Mater. Chem. A*, 2017, **5**, 12735–12739.
49 M. Retuerto, L. Pascual, F. Calle-Vallejo, P. Ferrer, D. Gianolio, A. G. Pereira, A. Garcia, J. Torrero, M. T. Fernandez-Diaz, P. Bencok, M. A. Pena, J. L. G. Fierro and S. Rojas, *Nat. Commun.*, 2019, **10**, 2041.
50 B. Hua, Y. F. Sun, M. Li, N. Yan, J. Chen, Y. Q. Zhang, Y. Zeng, B. S. Amirkhiz and J. L. Luo, *Chem. Mater.*, 2017, **29**, 6228–6237.
51 J. Liu, E. Jia, L. Wang, K. A. Stoerzinger, H. Zhou, C. S. Tang, X. Yin, X. He, E. Bousquet, M. E. Bowden, A. T. S. Wee, S. A. Chambers and Y. Du, *Adv. Sci.*, 2019, **6**, 1901073.
52 J. I. Jung, H. Y. Jeong, J. S. Lee, M. G. Kim and J. Cho, *Angew. Chem., Int. Ed.*, 2014, **53**, 4582–4586.
53 D. Zhang, Y. Song, Z. Du, L. Wang, Y. Li and J. B. Goodenough, *J. Mater. Chem. A*, 2015, **3**, 9421–9426.
54 G. Chen, Z. Hu, Y. Zhu, Z. G. Chen, Y. Zhong, H. J. Lin, C. T. Chen, L. H. Tjeng, W. Zhou and Z. Shao, *J. Mater. Chem. A*, 2018, **6**, 9854–9859.
55 Q. Wang, Y. Xue, S. Sun, S. Li, H. Miao and Z. Liu, *Electrochim. Acta*, 2017, **254**, 14–24.
56 D. Mierwaldt, S. Mildner, R. Arrigo, A. Knop-Gericke, E. Franke, A. Blumenstein, J. Hoffmann and C. Jooss, *Catalysts*, 2014, **4**, 129–145.
57 Y. Zhu, W. Zhou, J. Sunarso, Y. Zhong and Z. Shao, *Adv. Funct. Mater.*, 2016, **26**, 5862–5872.
58 Y. Pan, X. Xu, Y. Zhong, L. Ge, Y. Chen, J. M. Veder, D. Guan, R. O'Hayre, M. Li, G. Wang, H. Wang, W. Zhou and Z. Shao, *Nat. Commun.*, 2020, **11**, 2002.
59 J. Dai, Y. Zhu, Y. Zhong, J. Miao, B. Lin, W. Zhou and Z. Shao, *Adv. Mater. Interfaces*, 2019, **6**, 1801317.
60 B. Hua, M. Li, W. Pang, W. Tang, S. Zhao, Z. Jin, Y. Zeng, B. S. Amirkhiz and J. L. Luo, *Chem*, 2018, **4**, 2902–2916.
61 S. Peng, X. Han, L. Li, S. Chou, D. Ji, H. Huang, Y. Du, J. Liu and S. Ramakrishna, *Adv. Energy Mater.*, 2018, **8**, 1800612.
62 B. Xia, T. Wang, J. Ran, S. Jiang, X. Gao and D. Gao, *ACS Appl. Mater. Interfaces*, 2021, **13**, 2447–2454.
63 Q. Guo, X. Li, H. Wei, Y. Liu, L. Li, X. Yang, X. Zhang, H. Liu and Z. Lu, *Front. Chem.*, 2019, **7**, 224.
64 G. Fu, W. Li, J. Y. Zhang, M. Li, C. Li, N. Li, Q. He, S. Xi, D. Qi, J. L. MacManus-Driscoll, J. Cheng and K. H. Zhang, *Small*, 2021, **17**, 2006930.
65 Y. Dai, J. Yu, C. Cheng, P. Tan and M. Ni, *Chem. Eng. J.*, 2020, **397**, 125516.
66 D. Liu, P. Zhou, H. Bai, H. Ai, X. Du, M. Chen, D. Liu, W. F. Ip, K. H. Lo, C. T. Kwok, S. Chen, S. Wang, G. Xing, X. Wang and H. Pan, *Small*, 2021, 2101605.
67 J. T. Mefford, X. Rong, A. M. Abakumov, W. G. Hardin, S. Dai, A. M. Kolpak, K. P. Johnston and K. J. Stevenson, *Nat. Commun.*, 2016, **7**, 11053.
68 M. Pavone, A. B. Muñoz-García, A. M. Ritzmann and E. A. Carter, *J. Phys. Chem. C*, 2014, **118**, 13346–13356.
69 Z. Shen, Y. Zhuang, W. Li, X. Huang, F. E. Oropeza, E. J. M. Hensen, J. P. Hofmann, M. Cui, A. Tadich, D. Qi, J. Cheng, J. Li and K. H. L. Zhang, *J. Mater. Chem. A*, 2020, **8**, 4407–4415.
70 M. Qu, X. Ding, Z. Shen, M. Cui, F. E. Oropeza, G. Gorni, V. A. de la Peña O'Shea, W. Li, D.-C. Qi and K. H. L. Zhang, *Chem. Mater.*, 2021, **33**, 2062–2071.
71 S. Song, J. Zhou, J. Sun, S. Zhang, X. Lin, Z. Hu, J. Hu, L. Zhang and J. Q. Wang, *Chin. J. Catal.*, 2020, **41**, 592–597.
72 R. Liu, F. Liang, W. Zhou, Y. Yang and Z. Zhu, *Nano Energy*, 2015, **12**, 115–122.
73 S. She, J. Yu, W. Tang, Y. Zhu, Y. Chen, J. Sunarso, W. Zhou and Z. Shao, *ACS Appl. Mater. Interfaces*, 2018, **10**, 11715–11721.
74 V. Celorrio, L. Calvillo, E. Dann, G. Granozzi, A. Aguadero, D. Kramer, A. E. Russell and D. J. Fermín, *Catal. Sci. Technol.*, 2016, **6**, 7231–7238.

75 Y. Zhao, Y. Hang, Y. Zhang, Z. Wang, Y. Yao, X. He, C. Zhang and D. Zhang, *Electrochim. Acta*, 2017, **232**, 296–302.
76 N. Tsvetkov, Q. Lu, L. Sun, E. J. Crumlin and B. Yildiz, *Nat. Mater.*, 2016, **15**, 1010–1016.
77 D. He, G. He, H. Jiang, Z. Chen and M. Huang, *Chem. Commun.*, 2017, **53**, 5132–5135.
78 J. Reszczyńska, T. Grzyb, J. W. Sobczak, W. Lisowski, M. Gazda, B. Ohtani and A. Zaleska, *Appl. Catal., B*, 2015, **163**, 40–49.
79 Y. Sun, Z. Liu, W. Zhang, X. Chu, Y. Cong, K. Huang and S. Feng, *Small*, 2019, **15**, 1803513.
80 D. Neagu, G. Tsekouras, D. N. Miller, H. Menard and J. T. Irvine, *Nat. Chem.*, 2013, **5**, 916–923.
81 X. Liang, L. Shi, Y. Liu, H. Chen, R. Si, W. Yan, Q. Zhang, G. D. Li, L. Yang and X. Zou, *Angew. Chem., Int. Ed.*, 2019, **58**, 7631–7635.
82 C. Wang, L. Zeng, W. Guo, C. Gong and J. Yang, *RSC Adv.*, 2019, **9**, 35646–35654.
83 E. Y. Göl, A. Aytekin, E. E. Özkahraman and E. Karabudak, *J. Appl. Electrochem.*, 2020, **50**, 1037–1043.
84 N. Sun, H. Liu, Z. Yu, Z. Zheng and C. Shao, *RSC Adv.*, 2016, **6**, 13522–13530.
85 Y. Duan, S. Sun, S. Xi, X. Ren, Y. Zhou, G. Zhang, H. Yang, Y. Du and Z. J. Xu, *Chem. Mater.*, 2017, **29**, 10534–10541.
86 J. Sun, L. Du, B. Sun, G. Han, Y. Ma, J. Wang, H. Huo, P. Zuo, C. Du and G. Yin, *J. Energy Chem.*, 2021, **54**, 217–224.
87 Z. Li, L. Lv, J. Wang, X. Ao, Y. Ruan, D. Zha, G. Hong, Q. Wu, Y. Lan, C. Wang, J. Jiang and M. Liu, *Nano Energy*, 2018, **47**, 199–209.
88 Y. Jiang, Z. Geng, L. Yuan, Y. Sun, Y. Cong, K. Huang, L. Wang and W. Zhang, *ACS Sustainable Chem. Eng.*, 2018, **6**, 11999–12005.
89 Q. Luo, D. Lin, W. Zhan, W. Zhang, L. Tang, J. Luo, Z. Gao, P. Jiang, M. Wang, L. Hao and K. Tang, *ACS Appl. Energy Mater.*, 2020, **3**, 7149–7158.
90 V. Vats and A. Singhal, *Electroanalysis*, 2020, **33**, 618–626.
91 M. N. Grisolia, J. Varignon, G. Sanchez-Santolino, A. Arora, S. Valencia, M. Varela, R. Abrudan, E. Weschke, E. Schierle, J. E. Rault, J. P. Rueff, A. Barthelemy, J. Santamaria and M. Bibes, *Nat. Phys.*, 2016, **12**, 484–492.
92 K. Elumeeva, J. Masa, F. Tietz, F. Yang, W. Xia, M. Muhler and W. Schuhmann, *ChemElectroChem*, 2016, **3**, 138–143.
93 J. X. Flores-Lasluisa, F. Huerta, D. Cazorla-Amoros and E. Morallon, *J. Colloid Interface Sci.*, 2019, **556**, 658–666.
94 Y. Han, Z. Zhu, L. Huang, Y. Guo, Y. Zhai and S. Dong, *Nanoscale*, 2019, **11**, 19579–19585.
95 X. Liu, H. Gong, T. Wang, H. Guo, L. Song, W. Xia, B. Gao, Z. Jiang, L. Feng and J. He, *Chem. – Asian J.*, 2018, **13**, 528–535.
96 N. T. Suen, S. F. Hung, Q. Quan, N. Zhang, Y. J. Xu and H. M. Chen, *Chem. Soc. Rev.*, 2017, **46**, 337–365.
97 B. Han, A. Grimaud, L. Giordano, W. T. Hong, O. Diaz-Morales, L. Yueh-Lin, J. Hwang, N. Charles, K. A. Stoerzinger, W. Yang, M. T. M. Koper and Y. Shao-Horn, *J. Phys. Chem. C*, 2018, **122**, 8445–8454.
98 S.-L. Zhang, D. Cox, H. Yang, B.-K. Park, C.-X. Li, C.-J. Li and S. A. Barnett, *J. Mater. Chem. A*, 2019, **7**, 21447–21458.
99 P. Kolla, G. Nasymov, R. Rajappagowda and A. Smirnova, *J. Power Sources*, 2020, **446**, 227234.
100 Y. Liu, X. Kong, X. Guo, Q. Li, J. Ke, R. Wang, Q. Li, Z. Geng and J. Zeng, *ACS Catal.*, 2019, **10**, 1077–1085.
101 B. J. Kim, E. Fabbri, D. F. Abbott, X. Cheng, A. H. Clark, M. Nachtegaal, M. Borlaf, I. E. Castelli, T. Graule and T. J. Schmidt, *J. Am. Chem. Soc.*, 2019, **141**, 5231–5240.
102 M. S. Burke, S. Zou, L. J. Enman, J. E. Kellon, C. A. Gabor, E. Pledger and S. W. Boettcher, *J. Phys. Chem. Lett.*, 2015, **6**, 3737–3742.
103 X. Xu, C. Su, W. Zhou, Y. Zhu, Y. Chen and Z. Shao, *Adv. Sci.*, 2016, **3**, 1500187.
104 H. Sun, X. Xu, Z. Hu, L. H. Tjeng, J. Zhao, Q. Zhang, H.-J. Lin, C.-T. Chen, T.-S. Chan, W. Zhou and Z. Shao, *J. Mater. Chem. A*, 2019, **7**, 9924–9932.
105 Y. Lv, Z. Li, Y. Yu, J. Yin, K. Song, B. Yang, L. Yuan and X. Hu, *J. Alloys Compd.*, 2019, **801**, 19–26.
106 B. Hou, C. C. Wang, R. Tang, Q. Zhang, Z. Tan, X. Fan and X. Cui, *Nano*, 2020, **15**, 2050077.
107 X. Xu, Y. Chen, W. Zhou, Y. Zhong, D. Guan and Z. Shao, *Adv. Mater. Interfaces*, 2018, **5**, 1701693.
108 A. Grimaud, O. Diaz-Morales, B. Han, W. T. Hong, Y. L. Lee, L. Giordano, K. A. Stoerzinger, M. T. M. Koper and Y. Shao-Horn, *Nat. Chem.*, 2017, **9**, 457–465.
109 J. Ran, T. Wang, J. Zhang, Y. Liu, C. Xu, S. Xi and D. Gao, *Chem. Mater.*, 2020, **32**, 3439–3446.
110 Y. Zhu, Q. Lin, Z. Wang, D. Qi, Y. Yin, Y. Liu, X. Zhang, Z. Shao and H. Wang, *J. Energy Chem.*, 2021, **52**, 115–120.
111 B. Xia, T. Wang, X. Jiang, J. Li, T. Zhang, P. Xi, D. Gao and D. Xue, *J. Mater. Chem. A*, 2019, **7**, 4729–4733.
112 M. Li, L. Tao, X. Xiao, X. Lv, X. Jiang, M. Wang, Z. Peng and Y. Shen, *ChemCatChem*, 2018, **10**, 4119–4125.
113 Y. Sun, R. Li, X. Chen, J. Wu, Y. Xie, X. Wang, K. Ma, L. Wang, Z. Zhang, Q. Liao, Z. Kang and Y. Zhang, *Adv. Energy Mater.*, 2021, **11**, 2003755.
114 H. Lv, L. Lin, X. Zhang, Y. Song, H. Matsumoto, C. Zeng, N. Ta, W. Liu, D. Gao, G. Wang and X. Bao, *Adv. Mater.*, 2020, **32**, 1906193.
115 K. Chu, F. Liu, J. Zhu, H. Fu, H. Zhu, Y. Zhu, Y. Zhang, F. Lai and T. Liu, *Adv. Energy Mater.*, 2021, **11**, 2003799.
116 Y. Xu, X. Xu, N. Cao, X. Wang, X. Liu, M. Fronzi and L. Bi, *Int. J. Hydrogen Energy*, 2021, **46**, 10293–10302.